2022-11-18

The Winchcombe meteorite, a unique and pristine witness from the outer solar system

King, AJ

10.1126/sciadv.abq3925
Science Advances
American Association for the Advancement of Science (AAAS)

ATMOSPHERIC SCIENCE

The Winchcombe meteorite, a unique and pristine witness from the outer solar system

Ashley J. King[1,2,3†*], Luke Daly[4,5,6,7,3†*], James Rowe[2,3], Katherine H. Joy[8,3], Richard C. Greenwood[9], Hadrien A. R. Devillepoix[10], Martin D. Suttle[9,1,7], Queenie H. S. Chan[11,9], Sara S. Russell[1], Helena C. Bates[1], James F. J. Bryson[5], Patricia L. Clay[8], Denis Vida[12], Martin R. Lee[4], Áine O'Brien[4], Lydia J. Hallis[4], Natasha R. Stephen[13], Romain Tartèse[8], Eleanor K. Sansom[10], Martin C. Towner[10], Martin Cupak[10], Patrick M. Shober[14], Phil A. Bland[10], Ross Findlay[9], Ian A. Franchi[9], Alexander B. Verchovsky[9], Feargus A. J. Abernethy[9], Monica M. Grady[9], Cameron J. Floyd[4], Matthias Van Ginneken[15], John Bridges[16], Leon J. Hicks[16], Rhian H. Jones[8], Jennifer T. Mitchell[13], Matthew J. Genge[17], Laura Jenkins[4], Pierre-Etienne Martin[4], Mark A. Sephton[17], Jonathan S. Watson[17], Tobias Salge[1], Katherine A. Shirley[5], Rowan J. Curtis[5], Tristram J. Warren[5], Neil E. Bowles[5], Finlay M. Stuart[18], Luigia Di Nicola[18], Domokos Györe[18,19], Adrian J. Boyce[18], Kathryn M. M. Shaw[20], Tim Elliott[20], Robert C. J. Steele[21], Pavel Povinec[22], Matthias Laubenstein[23], David Sanderson[18], Alan Cresswell[18], Anthony J. T. Jull[24,25], Ivan Sýkora[22], Sanjana Sridhar[5], Richard J. Harrison[26], Francesca M. Willcocks[13], Catherine S. Harrison[1,8], Daniel Hallatt[15,27], Penny J. Wozniakiewicz[15], Mark J. Burchell[15], Luke S. Alesbrook[15], Aishling Dignam[15], Natasha V. Almeida[1], Caroline L. Smith[1,4], Brett Clark[1], Emma R. Humphreys-Williams[1], Paul F. Schofield[1], Luke T. Cornwell[15], Vassilia Spathis[15], Geraint H. Morgan[9], Mark J. Perkins[28], Richard Kacerek[29,3], Peter Campbell-Burns[29,3], Francois Colas[14,30], Brigitte Zanda[31,30], Pierre Vernazza[32,30], Sylvain Bouley[33,30], Simon Jeanne[14,30], Mike Hankey[34], Gareth S. Collins[17,3], John S. Young[26,7], Clive Shaw[26,7], Jana Horak[35,2,3], Dave Jones[29], Nick James[36], Steve Bosley[29], Alan Shuttleworth[2], Paul Dickinson[37], Ian McMullan[7], Derek Robson[36,29], Andrew R. D. Smedley[8,2,3], Ben Stanley[34], Richard Bassom[29,37], Mark McIntyre[29,37,3], Adam A. Suttle[7], Richard Fleet[29], Luc Bastiaens[34], Míra B. Ihász[38], Sarah McMullan[17,7,3], Sarah J. Boazman[39], Zach I. Dickeson[1], Peter M. Grindrod[1], Annemarie E. Pickersgill[4,18], Colin J. Weir[3], Fiona M. Suttle[3], Sarah Farrelly[40], Ieun Spencer[40], Sheeraz Naqvi[40], Ben Mayne[40], Dan Skilton[40], Dan Kirk[40], Ann Mounsey[3], Sally E. Mounsey[3], Sarah Mounsey[3], Pamela Godfrey[3], Lachlan Bond[3], Victoria Bond[3], Cathryn Wilcock[3], Hannah Wilcock[3], Rob Wilcock[3]

Direct links between carbonaceous chondrites and their parent bodies in the solar system are rare. The Winchcombe meteorite is the most accurately recorded carbonaceous chondrite fall. Its pre-atmospheric orbit and cosmic-ray exposure age confirm that it arrived on Earth shortly after ejection from a primitive asteroid. Recovered only hours after falling, the composition of the Winchcombe meteorite is largely unmodified by the terrestrial environment. It contains abundant hydrated silicates formed during fluid-rock reactions, and carbon- and nitrogen-bearing organic matter including soluble protein amino acids. The near-pristine hydrogen isotopic composition of the Winchcombe meteorite is comparable to the terrestrial hydrosphere, providing further evidence that volatile-rich carbonaceous asteroids played an important role in the origin of Earth's water.

INTRODUCTION

The early solar system comprised at least two isotopically distinct reservoirs separated by a barrier proposed to reflect the orbits of the proto-gas giants and/or location of snow lines (*1*, *2*). Small bodies that accreted late in the outer regions of the solar system and avoided high temperatures and melting are crucial for understanding the initial composition of the protoplanetary disk. Dynamical models and remote sensing observations suggest that primitive, volatile-rich asteroids originating in the outer solar system were scattered inward to the main asteroid belt by the giant planets (*3*, *4*). Carbonaceous chondrite meteorites are likely fragments of these asteroids and have volatile abundances and isotopic compositions that indicate that they played a key role in the delivery of water and biologically important molecules to Earth and other terrestrial planets (*5*). However, direct links between meteorites and their parent bodies are poorly constrained, with only four carbonaceous chondrite falls with pre-atmospheric orbits having been recovered to date (*6*–*9*). Most carbonaceous chondrites are fortuitous finds that lack information about their source region(s) in the solar system.

Recently, JAXA's Hayabusa2 and NASA's OSIRIS-REx missions have sampled the surfaces of the carbonaceous near-Earth asteroids Ryugu and Bennu, respectively. Both are rubble-pile asteroids thought to be derived from either the Eulalia or new Polana

collisional families that reside in the inner main belt [~2.1 astronomical units (AU) < a < 2.5 AU], although their original parent body(ies) probably formed beyond the orbit of Jupiter (*10*). Ryugu and Bennu have complex orbital histories and were potentially modified during transport from the outer solar system to their current locations at ~1 AU (*11*). In comparison, the Winchcombe CM ("Mighei-like") meteorite is the most widely observed carbonaceous chondrite fall to date and has a well-constrained pre-atmospheric orbit that confirms that it originated from an asteroidal source in the main belt. As the meteorite was recovered soon after landing, it also offers a near-pristine record of the composition of primitive asteroids. This combination of pre-atmospheric data with a fresh sample largely unmodified by the terrestrial environment makes the Winchcombe meteorite comparable to materials returned by space missions. Here, we report the orbital characteristics and results of coordinated laboratory analyses of the petrography and organic composition of the Winchcombe carbonaceous chondrite.

RESULTS

The Winchcombe fireball occurred at 21:54:16 (UT) on 28 February 2021 and was recorded by 16 dedicated meteor cameras (fig. S1 and table S1). The fireball was also captured on numerous doorbell and dashcam videos, and there were >1000 eyewitness accounts and reports of a sonic boom to the International Meteor Organization (IMO) and UK Meteor Observation Network (UKMON). The main mass (319.5 g) of the meteorite was discovered the next day in the town of Winchcombe, Gloucestershire, UK. The stone landed on a driveway, fracturing into a pile of dark millimeter- to centimeter-sized fragments and powder (Fig. 1) that was collected with the aid of rubber gloves and securely sealed within polyethylene bags only ~12 hours after the fall. Further stones were recovered in the local area over the following week by the public and during an organized search by members of the U.K. planetary science community (table S4). The largest intact piece of the Winchcombe meteorite is a 152.0-g fusion-crusted stone found on farmland on 6 March 2021 (Fig. 1C). In total, 531.5 g of material was recovered less than 7 days after the fall, when there was fog and dew on the ground but no rainfall in the area.

The pre-atmospheric orbit of the Winchcombe meteorite is similar to those reported for the C/CM chondrite Sutter's Mill (*7*) and CM chondrite Maribo (*8*), but distinct from the ungrouped carbonaceous chondrites Tagish Lake ($C2_{ung}$) (*6*) and Flensburg ($C1_{ung}$) (*9*) (Fig. 2 and table S2). Orbital analysis for Winchcombe, Sutter's Mill, and Maribo confirms that recent CM chondrite falls have a common source region, which is probably close to the 3:1 mean motion resonance with Jupiter in the main asteroid belt (a = 2.5 AU) (*12*). The orbits of both Sutter's Mill and Maribo had a Tisserand's parameter with respect to Jupiter [$T_J = 2.81 \pm 0.32$ (*7*) and 2.95 ± 0.11 (*8*), respectively], which tentatively implied that they were derived from Jupiter-family comets (T_J = 2 to 3) rather than asteroids ($T_J > 3$). However, a T_J value of 3.121 ± 0.006 for the Winchcombe meteoroid is consistent with an origin from an asteroid (*13*).

The low albedo and visible and near-infrared (IR) spectral properties of CM chondrites link them to the primitive Ch/Cgh- and B-type asteroids that are common in the middle of the main belt (2.5 AU < a < 2.8 AU) (*4*). The presence of phyllosilicates and/or ices on the surfaces of these asteroids is inferred from absorption bands in reflectance spectra at ~0.7 and/or ~3 μm and suggests that they accreted beyond the water snow line (*4*). Powdered interior fragments of the Winchcombe meteorite have a broadband albedo (4.09 ± 0.18%), spectral slopes, and 3-μm features consistent with remote observations of hydrated C-type asteroids (fig. S6).

Most meteorites spend millions of years between ejection from their parent bodies by collision in the main belt and arrival on Earth (*14*); however, CM chondrites typically have cosmic-ray exposure (CRE) ages that are <2 million years (Ma) old (*15*). Integrating the Winchcombe meteoroid's pre-atmospheric orbit in the past shows that it spent little time in near-Earth space [median near-Earth entry of ~0.08 Ma], while its short ^{21}Ne (center of the range measured in three samples is ~0.3 Ma) and ^{26}Al (0.27 ± 0.08 Ma) CRE ages are within the main cluster of exposure ages for CM chondrites (tables S6, S7, and S21) (*15*). This suggests that both the ejection of the Winchcombe meteoroid from a larger parent asteroid and its migration from the main belt to near-Earth space were near-contemporaneous events.

The perihelion distance of the Winchcombe meteoroid's orbit (~0.99 AU; table S2) was approximately twice as large as those for Sutter's Mill and Maribo, while orbital analysis shows that it likely remained at >0.7 AU throughout its history. This implies that the Winchcombe meteorite may have experienced less thermal processing from close passes to the Sun than other CM chondrite falls. The entry conditions of the Winchcombe meteoroid also differed from those of Sutter's Mill and Maribo, which were larger bodies (>1 m in diameter) that entered Earth's atmosphere at ~28 km s^{-1} (*7*, *8*). In contrast, the initial entry velocity of the Winchcombe meteoroid was 13.5 ± 0.01 km s^{-1}, and the entry mass based on the fireball observations was 13 ± 3 kg (fig. S4 and table S3), which is the

[1]Natural History Museum, London SW7 5BD, UK. [2]System for Capture of Asteroid and Meteorite Paths (SCAMP), UK. [3]UK Fireball Alliance (UKFAll), UK. [4]University of Glasgow, Glasgow G12 8QQ, UK. [5]University of Oxford, Oxford OX1 3AN, UK. [6]University of Sydney, Sydney 2006, NSW, Australia. [7]UK Fireball Network (UKFN), UK. [8]The University of Manchester, Manchester M13 9PL, UK. [9]The Open University, Milton Keynes MK7 6AA, UK. [10]Curtin University, Perth 6845, Australia. [11]Royal Holloway, University of London, Egham TW20 0EX, UK. [12]Western University, London N6A 3K7, Canada. [13]University of Plymouth, Plymouth PL4 8AA, UK. [14]Observatoire de Paris, Paris 75014, France. [15]University of Kent, Canterbury CT2 7NH, UK. [16]University of Leicester, Leicester LE1 7RH, UK. [17]Imperial College London, London SW7 2BP, UK. [18]Scottish Universities Environmental Research Centre (SUERC), East Kilbride G75 0QF, UK. [19]Isomass Scientific Inc., Calgary T2H 3A9, Canada. [20]University of Bristol, Bristol BS8 1RJ, UK. [21]University of St. Andrews, St. Andrews KY16 9TS, UK. [22]Comenius University, Bratislava 842 48, Slovakia. [23]INFN—Lab. Naz. Del Gran Sasso, Assergi 67100, Italy. [24]University of Arizona, Tucson, AZ 85721, USA. [25]Institute for Nuclear Research, Debrecen, Hungary. [26]University of Cambridge, Cambridge CB2 3EQ, UK. [27]Université de Lille, Lille 59000, France. [28]Anatune Ltd., Cambridge CB3 0NA, UK. [29]UK Meteor Observation Network (UKMON), UK. [30]Fireball Recovery and InterPlanetary Recovery (FRIPON), France. [31]Muséum National d'Histoire Naturelle, Paris 75005, France. [32]Aix-Marseille Université, Marseille 13007, France. [33]Université Paris-Saclay, Orsay 91405, France. [34]AllSky7 Meteor Camera Network. [35]Amgueddfa Cymru—National Museum Wales, Cardiff CF10 3NP, UK. [36]NEMETODE Network, UK. [37]Global Meteor Network (GMN). [38]Spire Global, Glasgow G3 8JU, UK. [39]European Space Research and Technology Centre (ESTEC), Keplerlaan 1, 2201 AZ Noordwijk, Netherlands. [40]Toucan Energy Ltd., London SE1 4PG, UK.
†These authors contributed equally to this work as co–first authors.
*Corresponding author. Email: a.king@nhm.ac.uk (A.J.K.); luke.daly@glasgow.ac.uk (L.D.)

Fig. 1. Images of Winchcombe meteorite. (**A**) The main mass of the Winchcombe meteorite recovered by the Wilcock family on 1 March 2021. (**B**) Example of a fragment from the driveway. (**C**) The largest intact stone found by M.B.Ihász. on 6 March 2021.

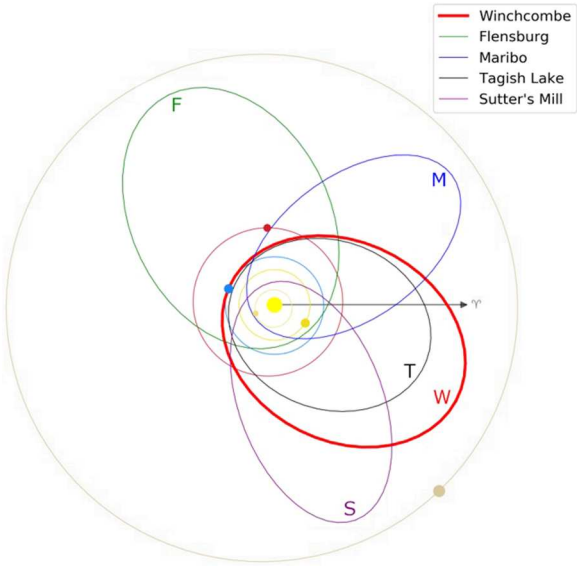

Fig. 2. Pre-atmospheric orbit of the Winchcombe (W) meteoroid compared with those of the carbonaceous chondrite falls Sutter's Mill (S) (*7*), Maribo (M) (*8*), Tagish Lake (T) (*6*), and Flensburg (F) (*9*). Planets are shown at the time of the Winchcombe fall.

lowest calculated for an instrumentally observed carbonaceous chondrite fall. The bulk density of the Winchcombe meteorite estimated from micro–x-ray computed tomography (XCT) is ~2090 kg m^{-3}, which, assuming a sphere, indicates an original body ~0.2 m in diameter. The analysis of cosmogenic nuclides in the Winchcombe meteorite further constrains the pre-atmospheric diameter to 0.3 ± 0.1 m and its mass to 30 ± 10 kg (table S7).

Modeling of the Winchcombe fireball indicates several fragmentations in the atmosphere at dynamic pressures of 0.02 to 0.6 MPa and a surviving mass of ~0.5 kg, close to the total mass of recovered meteorite stones. The maximum dynamic pressure of 0.6 MPa is the lowest ever determined for a recovered fall (*16*).

The classification of the Winchcombe meteorite as a CM carbonaceous chondrite is indicated by its bulk elemental abundances (tables S8 and S9), oxygen and titanium isotopic compositions (Fig. 3, fig. S9, and tables S10 to S12), and mineralogy and petrographic characteristics. Analysis of three fragments (~50 mg) by x-ray powder diffraction (XRD) indicates that the most abundant phases are phyllosilicates (>80 volume %; table S13).

Detailed observations of polished samples by scanning electron microscopy (SEM) show that the Winchcombe meteorite is a breccia, with multiple distinct lithologies identified (Fig. 4 and fig. S11). In the main lithology (>50% analyzed area, CM2.1), chondrules and calcium-aluminum–rich inclusions (CAIs) are near-complete pseudomorphs, with interiors replaced by phyllosilicates or calcite (fig. S12). The pseudomorphs often have well-preserved rims and are set within a matrix of phyllosilicate clumps and finer-grained materials (fig. S13). Transmission electron microscopy (TEM) analyses show that the phyllosilicates are Mg-rich (#Mg, ~0.63) and have d_{001} spacings of either ~0.62 to 0.70 nm (S-bearing) or ~0.70 to 0.74 nm (S-poor) that are characteristic of 1:1 layered T-O phyllosilicates such as serpentine-group minerals (fig. S15).

Most other lithologies contain tochilinite-cronstedtite intergrowths (TCIs) and carbonates (mainly calcite, although dolomite was also observed) with rims of phyllosilicates and/or Fe-sulfides (fig. S14). Anhydrous silicates and metal grains are rare. Magnetite is present as single isolated grains, framboids, and platelets, with first-order reversal curve (FORC) diagrams of the Winchcombe meteorite comparable to those of magnetite-rich chondrites (e.g., CI, Tagish Lake, and WIS 91600; fig. S16). The widespread presence of phyllosilicates, carbonates, and magnetite attests to low-temperature (<150°C) fluid-rock reactions on the parent asteroid (*20*). On the basis of the degree of chondrule and CAI replacement, and the abundance and composition of alteration products, these reactions were extensive and almost reached completion in most lithologies within the Winchcombe meteorite [petrologic subtype CM2.0–2.4 (*21*)].

In contrast to many other CM chondrites, samples of the Winchcombe meteorite contain almost pure trapped fractionated solar wind–derived noble gases, suggesting its origin from the near-surface regolith of its parent asteroid (figs. S7 and S22). Analysis by XCT shows that some lithologies have a pervasive set of parallel fractures, while others have a planar fabric produced by weak-to-moderate preferred shape alignment of chondrules and TCIs (fig. S17). Macroscale porosity of the void space is 0.6 to 4.2%, which typically manifests as fractures and interconnected pores. Brecciation was most likely facilitated by impacts and may record the catastrophic disruption of an initial, larger, hydrated planetesimal in the early solar system (*22*).

The water content of all CM chondrites is influenced by the terrestrial environment, including adsorption from the atmosphere and rapid formation of weathering products (*23*–*26*). A small aliquot (~45 mg) of the Winchcombe meteorite powder recovered from the driveway was characterized using thermogravimetric analysis (TGA) 5 days after the fall (table S17). Mass loss due to adsorbed water [2.4 weight % (wt %) between 20° and 100°C] was

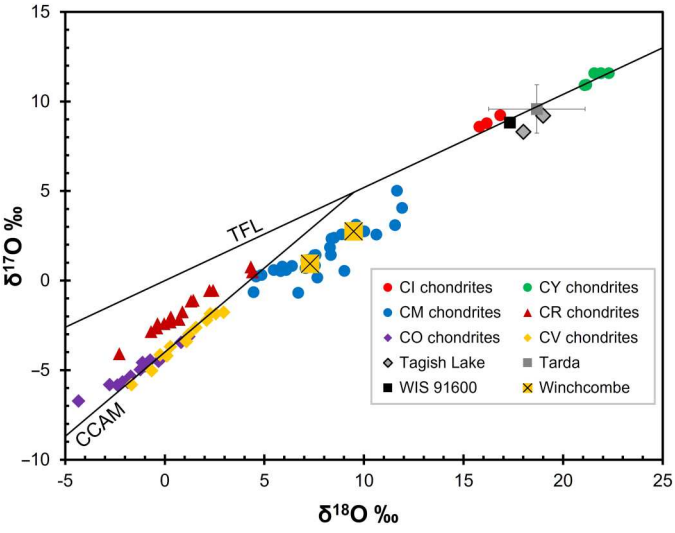

Fig. 3. Bulk oxygen isotopic composition of the Winchcombe meteorite. TFL, terrestrial fractionation line; CCAM, carbonaceous chondrite anhydrous mixing line. Oxygen data are from (*17*–*19*). Error bars for the Winchcombe meteorite are smaller than the symbols.

consistent with CM chondrite falls and finds. Meanwhile, the mass loss between 100° and 200°C was noticeably lower (0.6 wt %) than that of all other CM chondrites. This temperature region is associated with the decomposition of common weathering phases (e.g., sulfates) and shows the low terrestrial contamination of the Winchcombe meteorite (fig. S18). Three fragments split from a single driveway stone (0.11 g) were analyzed by hydrogen stepwise pyrolysis (fig. S19) within 1 month of the fall. Following the protocol of Lee *et al.* (*25*), data acquired at temperature steps of <200°C were not considered in the calculation of bulk water contents and δD values to remove any contribution from terrestrial adsorbed water. Thus, the hydrogen stepwise pyrolysis data gave an average water content of 10.5 ± 1.1 wt % and a bulk δD value of −142 ± 4‰ [relative to standard mean ocean water (SMOW); Fig. 5 and table S18]. These values are consistent with other highly altered CM chondrites and reflect exchange between isotopically light (δD ~−400‰) water and isotopically heavy (δD ~3500‰) organic matter (*5*). After including the Winchcombe meteorite, the average δD value of CM chondrite falls (n = 10) (*23*–*25*) is −102 ± 59‰. This supports recent claims that, of the available extraterrestrial materials, the hydrogen isotopic composition of CM chondrites most closely resembles that of Earth's hydrosphere (δD ~50 to −400‰) (*24*).

The elemental and isotopic abundances of carbon and nitrogen in two fresh samples (each ~5 mg) of the Winchcombe meteorite were characterized by stepped combustion 2 weeks after the fall. Overall, the release profiles were typical of CM chondrites and can mostly be attributed to organic matter in the matrix (figs. S20 and S21), at least some of which is highly volatile in nature, as shown by the analysis of species degassed from the Winchcombe meteorite (fig. S23). Stepped combustion analyses yielded an average bulk carbon abundance of 2.0 ± 0.1 wt % and $\delta^{13}C$ value of −1.7 ± 1.1‰, along with a bulk nitrogen abundance of 433.8 ± 20.3 parts per million (ppm) and $\delta^{15}N$ value of 16.7 ± 0.9‰ (Fig. 5). Previous CM chondrite falls tend to have

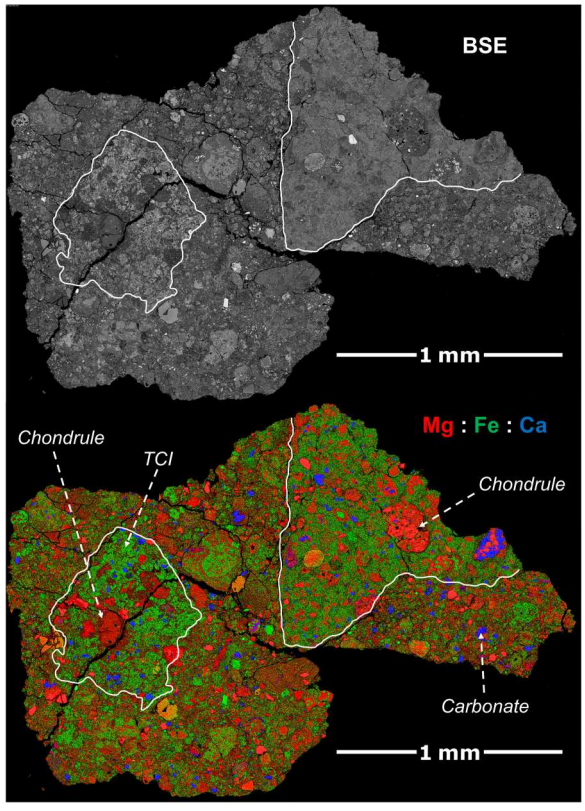

Fig. 4. BSE image and combined EDS map showing Mg, Fe, and Ca in a fragment (P30544) of the Winchcombe meteorite. The fragment contains three distinct lithologies (white lines), where the main phases are phyllosilicates (red/green), TCIs (green), carbonates (blue), and olivine (bright red).

bulk carbon abundances of ~2.2 wt %, lower $\delta^{13}C$ values (~−9‰), and higher nitrogen abundances (~0.1 wt %) and $\delta^{15}N$ values (~67‰). However, the low nitrogen abundance and $\delta^{15}N$ value of the Winchcombe meteorite are consistent with other highly altered CM chondrites and possibly result from the loss of a ^{15}N-rich organic component with greater degrees of aqueous alteration (*23*).

Low-voltage SEM characterization of fresh, unpolished fragments less than a week after the fall located several small carbon- and nitrogen-bearing regions with "globule-like" morphologies (Fig. 6A and fig. S24). The presence of nanoglobules similar to those reported in other carbonaceous chondrites was later confirmed by TEM (Fig. 6B). Soluble organic species, including protein amino acids, were investigated in the Winchcombe meteorite within 1 month of the fall, along with soil samples collected at the same time as Winchcombe. Fragments from both the driveway and farmland were analyzed by liquid chromatography–mass spectrometry (LC-MS), revealing lipids, fatty acids, fatty acyls, and fatty amines.

The macromolecular organic fraction of a driveway fragment was analyzed by gas chromatography–mass spectrometry (GC-MS) and found to contain structural units similar to those in other CM chondrites, including substituted benzenes and naphthalenes, various thiophenes, and polycyclic aromatic hydrocarbons. The most abundant amino acids detected in the Winchcombe meteorite were α-aminoisobutyric acid (467 ± 17 ng g^{-1}) and isovaline

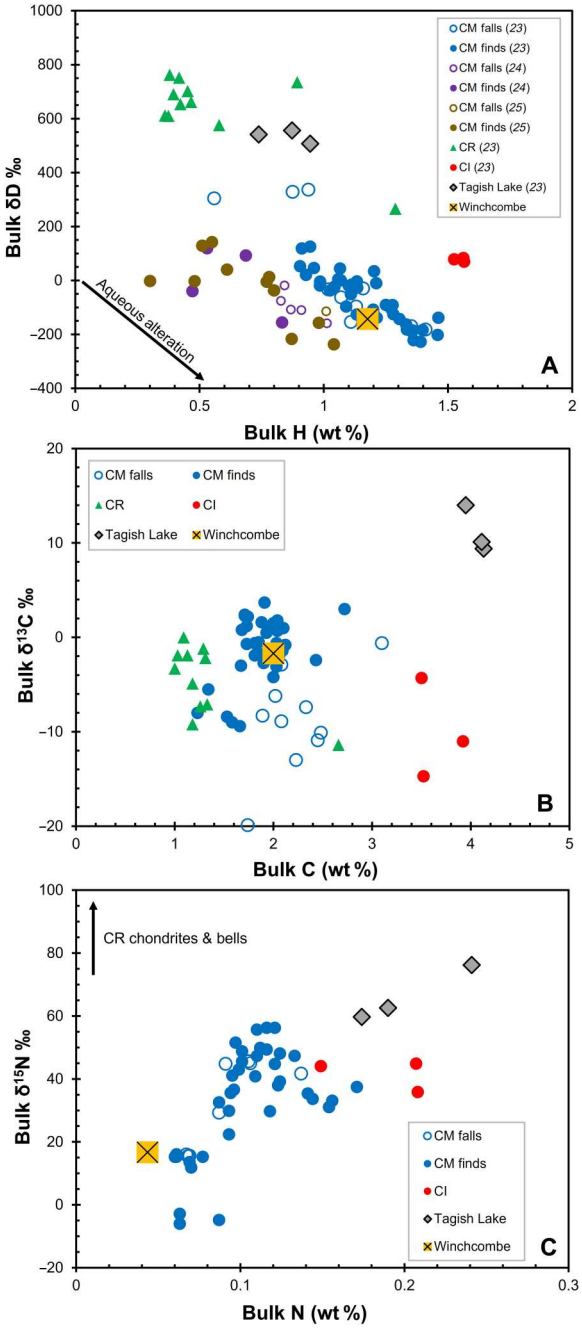

Fig. 5. Hydrogen (**A**), carbon (**B**), and nitrogen (**C**) compositions of the Winchcombe meteorite. Chondrite data are from (*23*–*25*). Error bars for the Winchcombe meteorite are smaller than the symbols.

(391 ± 17 ng g^{-1}; table S23). An extraterrestrial, abiotic origin for these compounds is supported by the racemic enantiomeric ratios detected in several protein and nonprotein amino acids (e.g., D/$L_{alanine}$ = 1.13 ± 0.16; D/$L_{isovaline}$ = 1.06 ± 0.15). The α-amino acids commonly found in CM chondrites likely formed through Strecker-cyanohydrin synthesis during aqueous alteration on the parent body (*27*). The total (free + bound peptide-like) amino acid abundance in the Winchcombe meteorite is 1132 ± 49 ng g^{-1}, which is lower than that of other CM falls, but in agreement

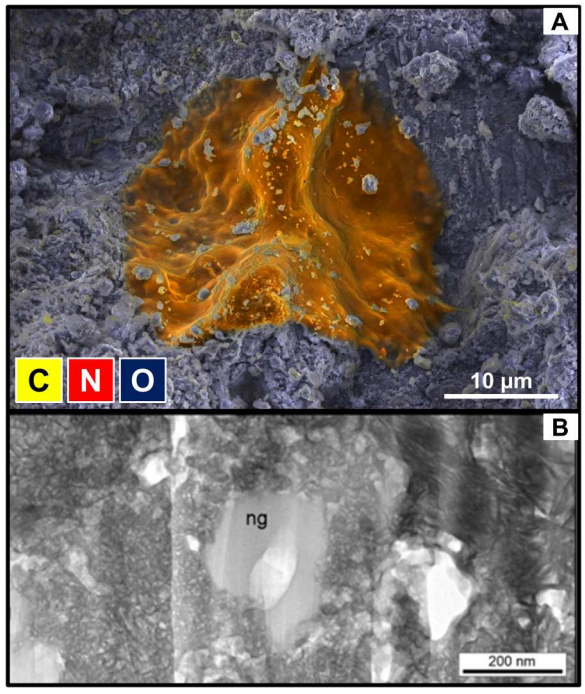

Fig. 6. Examples of carbon- and nitrogen-rich phases in the Winchcombe meteorite. (**A**) Combined secondary electron image and EDS map showing a C- and N-bearing globule-like morphology (orange) within the phyllosilicate-rich matrix (blue) of a fragment of the Winchcombe meteorite. Conditions: 6 kV, 158 pA, 38 kcps, 1360 × 960 pixels, and 49 nm pixel size. (**B**) Bright-field image of a nanoglobule (ng) that has been partially replaced by finely crystalline phyllosilicate on its left-hand side. The white areas are holes.

with highly altered Antarctic CM finds (*28*, *29*). Several CM chondrites contain an L-isovaline excess that has been proposed as an explanation for the bias toward L-amino acids in life on Earth (*30*, *31*); however, this was not observed in the Winchcombe meteorite. Nevertheless, prebiotic molecules such as amino acids are crucial components in the origin of life, and their presence in the fresh Winchcombe meteorite fall suggests that organic compounds could have been delivered to the early Earth by carbonaceous chondrites.

DISCUSSION

As a well-documented fall, the Winchcombe meteorite confirms the link between CM chondrites and hydrated main belt C-type asteroids that are thought to have originated in the outer solar system. This makes the Winchcombe meteorite complementary to asteroid regolith samples returned by the Hayabusa2 and OSIRIS-REx missions, although the parent body from which it was ejected likely never passed as close to the Sun as asteroids Ryugu and Bennu. Upon arrival on Earth, carbonaceous chondrites are highly susceptible to alteration in the terrestrial environment and extraterrestrial signatures can be modified within days (*26*). However, with the first material recovered within hours of the fall, facilitated by collaborative search efforts and citizen-science communities, the Winchcombe meteorite is the least terrestrially modified member of the CM chondrite group recovered to date. The Winchcombe meteorite, therefore, offers a near-pristine window into the geological

history of primitive asteroids and the chemical and dynamic evolution of volatiles in the early solar system.

MATERIALS AND METHODS

Fireball observations

The UK Fireball Alliance (UKFAll) is a collaboration of the six fireball and meteor camera networks in the United Kingdom including (i) the UKMON, which uses a mix of complementary metal-oxide semiconductor (CMOS) digital cameras and charged-coupled device (CCD)–based digital video cameras; (ii) the UK Fireball Network (UKFN), based on the digital single-lens reflex (DSLR) system developed by the Desert Fireball Network (DFN) in Australia (*32*); (iii) the System for the Capture of Asteroid and Meteorite Paths (SCAMP), a deployment of all-sky cameras from the French Fireball Recovery and InterPlanetary Observation Network (FRIPON) (*33*); (iv) the Network for Meteor Triangulation and Orbit Determination (NEMETODE), which uses CCD-based digital video cameras; (v) the Canadian-based Global Meteor Network (GMN), which uses CMOS digital video cameras (*34*); and (vi) the German-based AllSky7 network, with each site consisting of seven CMOS digital video cameras (*35*).

The Winchcombe fireball occurred at 21:54:16 (UT) on 28 February 2021 and lasted a little over 8 s. The skies over the United Kingdom were clear at the time, and eyewitness accounts and footage of the fireball captured on doorbell and dashboard cameras quickly appeared on social media channels or were uploaded to the IMO and UKMON websites. Several observers reported hearing a sonic boom.

Reflectance spectroscopy

Visible-? goniometer measurements

The broadband (0.35- to 1.25-μm) albedo of the Winchcombe meteorite was derived from bidirectional reflectance distribution function (BRDF) measurements taken using the Visible Oxford Space Environment Goniometer (VOSEG), a laboratory setup that can illuminate and measure the reflectance of a sample over a range of viewing angles (*36*). The BRDF was measured for a powdered sample of the Winchcombe meteorite (BM.2022,M1-22, 2.0 g) across 0° to 70° reflectance angles, in steps of 5°; at 15°, 30°, 45°, and 60° incidence angles; and at 0°, 90°, and 180° azimuthal angles. The data were then fitted using the Hapke BRDF model to enable constraints to be placed on the bulk scattering properties of the meteorite sample (*37*). The surface profile of the sample was characterized using an Alicona 3D (three-dimensional) instrument (fig. S5). Therefore, two of the free parameters within the model—the filling factor ϕ and the root mean square slope angle θ—could be set as $\phi = 0.65 \pm 0.02$ and $\theta = 16.11°$ (at 500 μm size scale). This enabled w, b, and h_S to be set as the three open parameters within the Hapke BRDF model least-squares Levenberg-Marquardt fitting function. The best-fit Hapke parameters were determined to be $w = 0.152 \pm 0.030$, $b = 0.633 \pm 0.064$, and $h_S = 0.016 \pm 0.008$. From the BRDF dataset, the broadband albedo value was calculated to be $A = 4.09 \pm 0.18\%$, which can be converted to hemispheric albedo by multiplying by π (*37*).

Spectrometer measurements

Visible to near-IR and mid-IR reflectance spectra of Winchcombe meteorite samples BM.2022,M1-91 and BM.2022,M2-41 were collected at the Planetary Spectroscopy Facility at the University of Oxford. Spectra were measured using a Bruker VERTEX 70v Fourier transform IR spectrometer using a diffuse reflectance accessory under vacuum (~2 hPa) at 4 cm^{-1} resolution, with an average of 150 scans all calibrated to a diffuse gold target. The shortest wavelength range (0.8 to 2.0 μm) was acquired using an InGaAs detector coupled with a VIS/quartz beam splitter, while an room temperature deuterated L-alanine doped triglycene sulphate (RT-DLaTGS) detector and wide-range beam splitter were used for the near- and mid-IR (2 to 30 μm). Because of features in the wide-range beam splitter, data at ~16 μm were excluded from the analysis.

Neon isotopic composition

The Ne isotopic composition of the Winchcombe meteorite was determined in two ~30-mg aliquots of homogenized powder (BM.2022,M2-36 and BM.2022,M4-7). Each sample was weighed into Pt foil, loaded in an ultrahigh-vacuum system, and baked overnight before analysis. Neon was released in four steps of increasing temperature using a 970-nm diode laser until a final melt step and reextraction to demonstrate complete degassing. Neon isotopes were measured using the electron multiplier procedure of a converted Thermo Fisher Scientific ARGUS VI noble gas mass spectrometer. Neon isotope data were corrected for blanks (<1%) and mass discrimination, and the reported uncertainties are 1σ. Full details of gas extraction, purification, and analysis procedures, as well as blank levels and the corrections for isobaric interferences, are described in (*38*).

Cosmogenic nuclides

Samples of the Winchcombe meteorite [BM.2022,M2-6, OE-2021-23 (1), and OE-2021-23 (7)] were analyzed nondestructively by low-background gamma-ray spectrometry. An additional sample (BM.2022,M2-40) was used for destructive analysis of ^{14}C (a soft beta-emitter) via high-sensitivity accelerator mass spectrometry (AMS). All samples were of irregular shape as they originated during a complex fragmentation process in the atmosphere during the meteorite fall, and they clearly showed effects of ablation due to their interaction with the atmosphere.

Gamma-ray spectrometry measurements were carried out at the Faculty of Mathematics, Physics and Informatics of Comenius University (Bratislava, Slovakia) and at the Laboratori Nazionali del Gran Sasso of the Italian Institute for Nuclear Physics (INFN-LNGS; Assergi, Italy). The low-background laboratory of Comenius University used high-purity germanium (HPGe) detectors of 70% (Princeton Gamma Tech (PGT), USA) and 50% (Canberra, Belgium) relative efficiency (for 1332.5-keV gamma-rays of ^{60}Co) placed in low-background shields situated in the basement of the three-story building. The larger shield, which is used for the 70% efficiency detector, has outer dimensions of 2 m by 1.5 m by 1.5 m and is composed of the following layers (from the outside to the inside): 10 cm of lead, 10 cm of electrolytic copper, 10 cm of polyethylene with boric acid, 0.1 cm of electrolytic copper, 0.1 cm of cadmium, and 1 cm of perspex. On the top, a layer of 12 cm of iron is added. The inner dimensions of the shield are 80 cm by 90 cm by 172 cm, where an extra shield made of electrolytic copper (12 cm by 20 cm by 30 cm) has been inserted to further decrease the background. The radon contribution to the detector background was decreased by flushing nitrogen gas through the inner copper shielding. A detailed description of the measuring procedures, energy and efficiency calibrations, and applied

corrections can be found in (*39*, *40*). The INFN-LNGS laboratory STELLA (Subterranean Low-Level Assay) operates 14 HPGe detectors, located deep underground with 1400 m of rock overburden (i.e., 3800 m of water equivalent), with additional ultralow-background shields (25 cm of lead and an inner liner of 5 cm of oxygen-free high-conductivity copper). Radon suppression was attained by flushing the closed shielding with ultrapure nitrogen (*41*). Both laboratories use, for efficiency determination of the HPGe detectors, dedicated programs based on the GEANT software package developed at CERN (*42*).

The AMS laboratory of the University of Arizona at Tucson carried out the ^{14}C analyses. Cosmogenic ^{14}C was extracted in a radio frequency (RF) induction furnace in a flow of oxygen, and passing the gases evolved over a CuO furnace to ensure conversion to CO_2. This gas was collected and measured volumetrically. The CO_2 was then converted to graphite and analyzed on a 3-MV National Electrostatics Corporation AMS machine. The full procedure for ^{14}C measurements is given in (*43*).

The database on radionuclide decay characteristics (*44*) was used for activity calculations. The uncertainties of results were mainly due to counting statistics, which were typically below 10%. The measuring time of gamma-ray spectrometry analysis was from 30 to 48 days, depending on the mass of the analyzed samples. Regular analysis of International Atomic Energy Agency (IAEA) and National Institute of Standards and Technology (NIST) reference materials and participation in intercomparison exercises guarantee to maintain a good quality of results.

Bulk element abundances

Major and trace element abundances of the powdered Winchcombe meteorite samples BM.2022,M1-91 and BM.2022,M2-41 were determined by inductively coupled plasma optical emission spectroscopy (ICP-OES) and ICP-MS in the Imaging and Analysis Centre (IAC) at the Natural History Museum (NHM). For major element analysis, ~40 mg of each powdered sample was pretreated with 0.5 ml of concentrated NHO_3 and fused with 120 mg of $LiBO_2$ in a Pt/Au crucible to produce a flux. This was then dissolved in 0.64 M HNO_3 before element abundances were measured in triplicate using a Thermo Fisher Scientific iCap 6500 Duo ICP-OES instrument, which was calibrated using a range of certified reference materials (CRMs) prepared in the same way. The standards BE-N (basalt, Groupe International de Travail) and JG-1 (granodiorite, Geological Survey of Japan) were analyzed as unknowns as a measure of accuracy.

To determine trace element abundances, a further ~40 mg of each powder was digested in HF + $HClO_4$ + HNO_3 and analyzed in triplicate using an Agilent 8900 ICP-QQQ-MS instrument. The instrument was optimized to reduce interferences by tuning CeO+/Ce+ and Ba++/Ba+ to <1%. The accuracy of analyses was monitored by measuring CRMs BCR-2 [basalt, U.S. Geological Survey (USGS)] and SY-2 (syenite, Canadian Certified Reference Material Project).

Oxygen isotopes

Oxygen isotopic analysis of the Winchcombe meteorite was undertaken at the Open University, UK using an IR laser-assisted fluorination system [e.g., (*45*)]. For the analysis, ~150-mg fragments extracted from samples BM.2022,M1-85 and BM.2022,M1-86 were powdered and homogenized.

All of the oxygen isotope analyses of the Winchcombe meteorite were run in modified "single shot" mode (*46*). This involved loading a single aliquot (~2 mg) of the homogenized powder into one of the wells of a nickel sample block. The sample was overlain by a ~1-mm-thick, 3-mm-diameter internal BaF_2 window to retain the sample during laser reaction. In a second well, a 2-mg aliquot of the internal obsidian standard was loaded without a BaF_2 window. The nickel sample block was then placed into the two-part laser chamber, which was made vacuum tight using a compression seal with a copper gasket and quick-release KFX clamp [e.g., (*45*)]. A 3-mm-thick BaF_2 window at the top of the chamber allows simultaneous viewing and laser heating of the samples.

Before analysis, the sample chamber was heated overnight under vacuum to a temperature of ~95°C to remove any adsorbed moisture. Following overnight heating, the chamber was allowed to cool to room temperature, and then the flexi sections that had been brought up to atmosphere during the sample loading procedures were purged using three aliquots of BrF_5 to remove any moisture. The sample chamber itself was kept closed during this procedure to avoid pre-reactions. Following these "flexi" blanks, the sample chamber was opened and a further single 5-min BrF_5 blank was undertaken to reduce and eliminate any residual moisture adsorbed onto the sample chamber walls. The oxygen isotope composition of this blank was analyzed using the MAT 253 microvolume facility. Following this blank analysis, the sample itself was run.

Sample heating in the presence of BrF_5 was carried out using a Photon Machines Inc. 50-W IR CO_2 laser (10.6 μm) mounted on an *X*-*Y*-*Z* gantry. Reaction progress was monitored by means of an integrated video system. After fluorination, the released O_2 was purified by passing it through two cryogenic nitrogen traps and over a bed of heated KBr to remove any excess fluorine. The isotopic composition of the purified oxygen gas was analyzed using a Thermo Fisher Scientific MAT 253 dual-inlet mass spectrometer with a mass resolving power of ~200. A postreaction blank was run following the analysis of the Winchcombe meteorite, and finally, the internal obsidian standard was fluorinated, and its oxygen isotope composition was determined.

Overall system precision, as defined by replicate analyses of the internal obsidian standard, is ±0.053‰ for $\delta^{17}O$, ±0.095‰ for $\delta^{18}O$, and ±0.018‰ for $\Delta^{17}O$ (2σ) (*47*). Oxygen isotopic analyses are reported in standard δ notation, where $\delta^{18}O$ value has been calculated as $\delta^{18}O = [(^{18}O/^{16}O)_{Sample}/(^{18}O/^{16}O)_{VSMOW} - 1] \times 1000$ (‰), and, similarly for $\delta^{17}O$, using the $^{17}O/^{16}O$ ratio. VSMOW is the international standard Vienna SMOW. $\Delta^{17}O$ value, which represents the deviation from the terrestrial fractionation line, has been calculated as follows: $\Delta^{17}O = \delta^{17}O - 0.52 \times \delta^{18}O$.

Titanium isotopes

A fragment of the Winchcombe meteorite (BM.2022,M3-16) was powdered using an agate mortar and pestle and digested in a 1:4 mixture of 29 M HF to 15 M nitric acid at 140°C in a 60-ml Savillex perfluoroalkoxy (PFA) beaker for >3 days and then dried at 110°C. The residue was redissolved in 15 ml of aqua regia in a 20-ml PFA beaker before refluxing in a Parr bomb for 7 days at 200°C to ensure complete dissolution of acid-resistant phases.

To isolate Ti, the sample underwent three stages of liquid chromatographic separation. The first consisted of an anionic resin column (Bio-Rad AG-1-X8, 100- to 200-mesh Cl form) to remove Fe using 6 M HCl. The second consisted of a cationic resin column

(Bio-Rad AG-50W-X12) from which Ti was eluted, plus other "high field strength" elements (e.g., Zr, Hf, Nb, and Ta) and Al, using 0.5 M HF, while the majority of matrix elements remained on the column. The final column consisted of an anionic resin, as in the first stage, eluting only Ti with a mixture of acetic acid, hydrogen peroxide, and nitric acid. This results in the separation of Ca, V, and Cr from Ti such that the final Ca/Ti, V/Ti, and Cr/Ti ratios were all <1:1000. The complete procedural blanks, including dissolution, produced <3 ng of Ti, which is negligible for the mass of the Winchcombe meteorite analyzed.

Titanium isotope ratios were measured by the Bristol Isotope Group at the University of Bristol on a Thermo Fisher Scientific Neptune MC-ICP-MS (s/n 10002) with a Jet-sample and X-skimmer cone combination. Samples dissolved in 0.3 M HNO_3 enter the plasma through an Aridus desolvating nebulizer using an Ar sweep gas with additional N_2 for increased sensitivity. Sample solution uptake rates vary between 40 and 50 μl min^{-1}. The Winchcombe meteorite sample was analyzed in "medium resolution" ($M/\Delta M > 6000$, where ΔM is the peak width between 5 and 95% intensity). The five Ti isotopes were measured alongside the intensities of $^{90}Zr^{2+}$, $^{51}V^{+}$, $^{52}Cr^{+}$, and $^{44}Ca^{+}$, which were monitored to track possible elemental interferences on ^{46}Ti, ^{48}Ti, and ^{50}Ti. Beam collection occurred in a "dynamic" mode, consisting of two magnetic settings with integration times of 8.4 s and a magnet setting time of 3 s. The main step collected $^{90}Zr^{2+}$, $^{46}Ti^{+}$, $^{47}Ti^{+}$, $^{48}Ti^{+}$, $^{49}Ti^{+}$ (axial mass), $^{50}Ti^{+}$, $^{51}V^{+}$, and $^{52}Cr^{+}$. The second step, measured every 10 main integration cycles, collected $^{44}Ca^{+}$ and $^{47}Ti^{+}$ (axial mass). Both steps require the measurement mass to be offset from the center of mass onto a "peak shoulder" to avoid molecular interferences, e.g., $^{36}Ar^{14}N^{+}$, $^{40}Ar^{12}C^{+}$, and $^{12}C^{16}O_2^{+}$. The beam intensities of all isotopes were measured using amplifiers with 10^{11}-ohm feedback resistors, excluding $^{90}Zr^{2+}$, which used an amplifier with a 10^{13}-ohm resistor, and $^{48}Ti^{+}$, which used an amplifier with a 10^{10}-ohm resistor.

The sample and standards were run at concentrations of 200 ng ml^{-1} (which yield ~2×10^{-10} A on $^{48}Ti^{+}$) and measured over 10 repeats of single blocks of 40 integrations. Instrumental blanks, usually <1% of the Ti signal, were measured before and after each block and subtracted from intermediate samples and standards. Mass-dependent fractionation was corrected by internal normalization using the exponential law and assuming a constant $^{49}Ti/^{47}Ti$ ratio of 0.749766 (*48*). Interferences of Ca, V, and Cr were also corrected (*49*–*51*). Each sample analysis was bracketed by a measurement of a standard solution of the same concentration, which, in this case, is the NIST-3162a standard reference material (SRM). Relative deviations of internally normalized Ti isotope ratios of the samples from a linear fit to internally normalized Ti isotope ratios of the bracketed NIST-3162a SRM were used to calculate $\Delta'^{X/47}Ti_{49/47}$ (reported in ppm). The reported values and errors are the mean and 2 SE of 10 repeat measurements in a single session. The mean and 2 SE reported values for $\Delta'^{46/47}Ti_{49/47}$, $\Delta'^{48/47}Ti_{49/47}$, and $\Delta'^{50/47}Ti_{49/47}$ from the same session for a BCR-2 basalt reference material were 1 ± 5, 2 ± 4, and 2 ± 10 ppm, respectively.

Chromium isotopes

A sample of the Winchcombe meteorite (BM.2022,M3-33) was crushed to a fine powder using an agate pestle and mortar. Approximately 20 mg was weighed into a 5-ml Savillex Teflon high-pressure vessel and dissolved in a 2:1 mixture of 29 M HF and 15.4 HNO_3 at 160°C for 3 days. The meteorite sample was dissolved alongside geostandard USGS DTS2B. After dissolution, the samples were evaporated to close to a gel, redissolved in 6 M HCl to avoid the formation of insoluble fluorides, and then dried. They were redissolved in repeated steps of 6 M HCl and 7 M HNO_3 until fully dissolved in solution.

Chromium was purified using a two-stage ion exchange procedure [e.g., (*52*)]. The first stage column was 4 ml of AG50W x8 in 1 M HCl; the samples were heated at 100°C for more than 18 hours in concentrated HCl and then diluted to 1 M HCl immediately before loading onto precleaned and preconditioned resin, and Cr was eluted with washes of 1 M HCl. Samples were dried and treated with concentrated HNO_3 to remove organics.

Next, the samples were dissolved in 0.5 M HNO_3:0.05% H_2O_2 and allowed to equilibrate for 5 days. Solutions were then loaded onto 400 μl of precleaned and preconditioned AG50W x8. Matrix elements were eluted with washes of 1 M HNO_3 followed by elution of Cr with 6 M HCl. The samples were further dried and treated with concentrated HNO_3 to remove organics and prepare for analysis. Before analysis, sample solutions were checked for adequate matrix separation and yield by analysis using an Agilent 8900 triple quad. The yield of the whole procedure was within an error of 100%, and the total procedural blank was <40 ng of Cr and negligible compared to the ~20 μg of Cr in the smallest samples.

Samples were measured using a Thermo Fisher Scientific Finnigan Neptune Plus MC-ICP-MS in the STAiG laboratory at the University of St. Andrews. The samples were aspirated using a nebulizer tip of 70 μl min^{-1} into an ESI Apex Omega desolvating nebulizer. Solutions were diluted to approximately 2 ppm, matched within 5% to the bracketing standard, with the full analytical session consuming 8 to 10 μg of Cr per sample. A standard sample cone was used with an x-type high-sensitivity skimmer cone. Measurements were made in high-resolution mode with $m/\Delta m > 8000$, yielding a sensitivity of 25 V/ppm of ^{52}Cr. Beams of ^{49}Ti, ^{50}Cr, ^{51}V, ^{52}Cr, ^{53}Cr, ^{54}Cr, and ^{56}Fe were simultaneously collected using cups L4, L2, L1, C, H1, H2, and H4. Each was connected to amplifiers with 10^{11}-ohm feedback resistors, except the cup collecting ^{52}Cr with a 10^{10}-ohm feedback resistor and L1 collecting ^{51}V with a 10^{12}-ohm feedback resistor. Samples and standards were 100 cycles of 8.439 s, and blanks were 50 cycles of 4.197 s.

Peak center routines were performed before each sample and standard measurement to monitor and correct for magnet drift. The measurement position was offset to the low mass side of the peak to resolve molecular interferences, and the position of the peak edge and interferences was verified by peak flat measurements before each analytical session. All sample measurements were bracketed by on-peak zero blank measurements and bracketing standard NIST SRM 979. Interference contributions from ^{50}Ti and ^{50}V on ^{50}Cr and ^{54}Fe were calculated from ^{49}Ti, ^{51}V, and ^{56}Fe, respectively. These were within the ranges for which these corrections can be accurately applied (*53*).

The degree of mass-dependent fractionation of the interfering isotope ratios was estimated from the $^{50}Cr/^{52}Cr$ ratio, and the interference ratios were adjusted accordingly before the interference signals were subtracted from the Cr isotope signals. Samples and standards were corrected for mass-dependent fractionation using the $^{50}Cr/^{52}Cr = 0.051859$ (*51*) ratio and the exponential law. Samples were corrected for nonexponential drift and cup factors by calculating the parts per 10,000 differences from the bracketing

standard, yielding ε^{53}Cr and ε^{54}Cr. Because of an issue in the detector electronics, occasional outliers were present on only the largest beam (^{52}Cr), which were often very large and resulted in >5σ outliers in the processed ratios. These did not influence the accuracy of the resulting data as they affected samples and standard alike but did artificially reduce the precision. The outliers were removed with a 3.25σ outlier rejection on the normalized ^{53}Cr/^{52}Cr ratio. This level of rejection would have no effect on the data if no outliers were present.

The reproducibility of the resulting data was estimated using a pooled dataset (n = 26), yielding 2 SD external precision of 6.4 ppm for ε^{53}Cr and 16.9 ppm for ε^{54}Cr on a single measurement and 3.2 ppm for ε^{53}Cr and 8.4 ppm for ε^{54}Cr 2se on a typical sample of n = 4. The accuracy of the analyses was verified with geostandard DTS2B, which was within the analytical uncertainty of previously reported ratios (*53*).

X-ray diffraction

The mineralogy of the Winchcombe meteorite was initially characterized on 9 March 2021 using a PANalytical X'Pert Pro scanning x-ray diffractometer at the NHM. Approximately ~5 mg of the powder BM.2022,M1-88 was mixed with several drops of acetone and deposited as a thin smear on a zero-background substrate. An XRD pattern of the sample was then collected using Co Kα radiation from 3° to 120° with a step size of 0.02° and time per step of 6.5 s, giving a total measurement time of ~12.5 hours. Mineral phases were identified using the International Centre for Diffraction Data (ICDD) database (PDF-2).

The modal mineralogy of ~50-mg aliquots of three powdered (grain size, <50 μm) samples (BM.2022,M1-91 and BM.2022,M2-41, also analyzed by IR spectroscopy and ICP-MS; BM.2022,M2-36, also analyzed for neon) was determined in May and June 2021 using an Enraf-Nonius PDS120 XRD equipped with an INEL curved 120° position-sensitive detector (PSD) at the NHM. The PSD is in a static geometry relative to the primary x-ray beam and sample, meaning the only moving part of the instrument is the sample stage, which is rotated throughout an analysis. Each powder was packed into an aluminum sample well using the sharp edge of a spatula to minimize preferred crystal alignments and then analyzed using Cu Kα radiation. PSD-XRD patterns of the Winchcombe meteorite samples were collected for 16 hours, and patterns of mineral standards were acquired under the same analytical conditions for 30 min.

Mineral abundances were calculated from the PSD-XRD patterns using a profile-stripping method, whereby the pattern of a mineral standard was initially scaled to the same measurement time as the meteorite samples (e.g., ×32). The mineral standard pattern was then reduced by a factor to fit its intensity in the diffraction pattern of a meteorite before being subtracted to leave a residual pattern. This process was repeated for all phases present in the meteorites, resulting in final residuals with zero counts and the fit factors summing to one. The fit factors were corrected for relative differences in x-ray absorption to give final volume fractions in the meteorites. The detection limit was ~0.5 to 1.0 volume %, and the uncertainties were ~0.5 to 5 volume % depending on the phase.

Petrographic observations

Two polished sections (P30423 and P30424) of the Winchcombe meteorite were prepared (without water) at the NHM and characterized using SEM and energy-dispersive spectrometry (EDS) in March to July 2021. Secondary and backscattered electron (BSE) images, EDS point spectra, and large-area high-resolution EDS elemental maps were acquired under high vacuum using a ZEISS EVO 15LS SEM equipped with an Oxford Instruments AZtec EDS system and 80-mm^2 X-Max silicon-drift detector (SDD) based on the IAC of the NHM. Whole-section EDS maps were collected with a spatial resolution of ~1.9 μm/pixel at an accelerating voltage of 20 kV and beam current of 3 nA, resulting in output count rates of >50 kcps and dead times of ~30 to 60%.

All EDS spot analyses were performed at a fixed working distance of 10.0 mm. An accelerating voltage of 20 kV and beam current of 1.5 nA resulted in an output count rate of ~40 to 60 kcps for silicate minerals. Before analysis, the EDS system was calibrated using a polished cobalt metal reference sample. Standards-based quantification was performed using the X-windows Phase Plane (XPP) matrix correction routine (*54*). For silicate minerals, quantification was performed using the "oxygen by stoichiometry" routine, while for carbonate minerals the "carbon by difference" and, for sulfides and metals, the "all elements" routines were used. The accuracy and precision for major rock-forming silicate cations were cross-checked against analyses on the Smithsonian Kakanui augite reference sample, for which the composition is known from wet chemistry. Element detection limits were on the order of 0.1 to 0.3 wt %.

A further 14 polished sections of the Winchcombe meteorite were prepared and characterized using SEM (table S14). Polished sections P30540 and P30552 were investigated at the University of Glasgow using a Zeiss Sigma field-emission SEM (FE-SEM) equipped with an Oxford Instruments X-Max EDS SDD and the AZtec/INCA software package. BSE images were acquired at an accelerating voltage of 20 kV and beam current of ~1 nA, and quantitative chemical spot analyses of individual mineral grains at 20 kV and ~2 nA. P30541 was studied at the University of Manchester using an FEI Quanta 650 FE-SEM operated under high vacuum. BSE images, EDS spectra, and elemental EDS x-ray maps were obtained with an accelerating voltage of 20 to 25 kV and beam currents of 3 to 6 nA. P30542 was studied at the University of Kent using a Hitachi S3400. Quantitative chemical analyses were acquired using an Oxford Instruments X-Max EDS SDD operated through the INCA software package. BSE images were obtained with an accelerating voltage of 20 kV and beam current of ~20 nA, and a combination of area and spot analyses was used to characterize individual minerals and fine-grained matrix. P30543 was studied using an FEI Quanta 650 FE-SEM at the University of Leicester Advanced Microscopy Facility. BSE images and EDS chemical compositions were acquired with an accelerating voltage between 5 and 20 kV and using Oxford Instruments AZtec software. P30545 was investigated by the Plymouth Electron Microscopy Centre at the University of Plymouth using a JOEL 7001F FE-SEM coupled with an Oxford Instruments X-Max 50-mm^2 EDS detector. BSE images were acquired using an accelerating voltage of 20 kV and beam current of 5 nA, and both spot analyses and larger-area x-ray elemental maps were collected using Oxford Instruments AZtec software. Last, the fusion crust in P30551, P30554, and P30555 was characterized using a Hitachi TM4000Plus at Imperial College, London, with BSE images and x-ray element maps acquired at 20 kV.

Transmission electron microscopy

Thin lamellae were cut and extracted from polished sections of the Winchcombe meteorite using an FEI Helios Plasma focused ion beam (FIB) instrument at the University of Glasgow and an FEI Quanta 200 3D FIB-SEM at the University of Leicester Advanced Microscopy Centre. In both cases, the protocol followed was similar to that outlined in (*55*). Briefly, the region of interest was initially coated with a ~1-μm-thick bar of Pt deposited by a gas injection system to protect the sample. Lamellae were then milled to a thickness of ~1 mm, before being extracted using an in situ micromanipulator and welded to a copper grid using platinum. After further milling to a thickness of ~100 nm, the lamellae were studied using TEM.

Lamellae from the matrix and fine grained rims (FGRs) within the polished sections P30540 and P30552 were initially characterized using an FEI T20 TEM at the University of Glasgow. An accelerating voltage of 200 kV was used to obtain diffraction-contrast images, high-resolution images, and selected-area electron diffraction (SAED) patterns from the lamellae. High-angle annular dark-field images and quantitative chemical analysis were also acquired at 200 kV using a JOEL ARM200F FE scanning TEM (STEM). For the analytical work, the x-ray spectra were acquired and processed using a Bruker Quantax EDS system with a 60-mm^2 SDD operating the Esprit V2.2 software. In addition, high-resolution TEM imaging, calibrated STEM-EDS, and lattice spacing measurements of serpentine-like phases in lamellae extracted from polished section P30543 were performed mostly using a JEOL 2100 TEM at the University of Leicester Advanced Microscopy Facility, as well as additional measurements using the JOEL 2100+ TEM at the University of Nottingham. Analyses used the Gatan Micrograph and Oxford Instruments AZtec software packages.

Bulk magnetic properties

A MicroMag 2900 Series alternating gradient magnetometer (AGM) at the University of Cambridge was used to measure hysteresis loops, DC demagnetization (DCD) curves, and FORC diagrams of chips taken from the Winchcombe meteorite samples BM.2022,M1-95 (3.3 mg) and BM.2022,M3-32 (11.4 mg). The FORC diagrams of the Winchcombe meteorite samples were compared quantitatively to those of CI and CM chondrites using principal components analysis [PCA; (*56*)]. In addition, MFK1-FA MultiFunction KappaBridge was used to measure the mass-specific magnetic susceptibility of 80.2- and 75.3-mg chips of BM.2022,M1-95 and BM.2022,M3-32, respectively.

Hysteresis loop measurements were conducted using an applied saturation field of 1 T, an averaging time of 200 ms, and a field increment of 10 mT. Paramagnetic adjustment was conducted to remove the effect of paramagnetic minerals in the samples. DCD curves were measured using an applied saturation field of 1 T, an initial field of 0 T, a maximum reverse applied field of −500 mT, and an averaging time of 1 s. A nonlinear field sequence was used with 150 points measured.

FORC diagram measurements were conducted using a saturating field of 1 T, a field-step size of 2.09 mT, and an averaging time of 275 ms. Three hundred FORCs were measured for each sample. The FORC diagrams were processed using the VARIFORC approach (*57*) within the FORCinel software package (*58*). During smoothing, a value of 0.2 was used for the horizontal and vertical lambda values (λ). Vertical ridge, central ridge, horizontal smoothing, and vertical smoothing parameters of 8, 5, 12, and 12 and 6, 6, 10, and 10 were used for chips BM.2022,M1-95 and BM.2022,M3-32, respectively. PCA was conducted on the processed FORC diagrams using the FORCem software package along with CM1 and CI1 chondrites (*56*, *59*).

Mass-specific magnetitic susceptibility measurements were conducted using an AC field amplitude of 200 A m^{-1} and a frequency of 976 Hz. Five measurements of each chip were taken, and the average was recorded.

Computed tomography

The internal and external features of 20 fragments of the Winchcombe meteorite (<0.01 to 0.36 g) were imaged using micro-XCT in July and August 2021 in the IAC of the NHM. For analysis, fragments were mounted in gel capsules with supporting foam and loaded into modified pipettes (~7 mm in diameter; one to two fragments per pipette), which were then fixed onto the stage of a cabinet-based industrial Zeiss Xradia Versa 520 CT system. X-rays were generated from a tungsten source using a voltage of 70 to 130 kV and a current of 76 to 87 μA. Appropriate x-ray source filtration was used to help reduce beam hardening effects.

For each fragment, a total of 1601 to 3201 projections were collected while it was rotated by 360°. The center shift during stage rotation was corrected in postprocessing using the Zeiss Reconstructor software. Each projection was magnified by a 4× or 0.4× objective lens and then recorded using a 2000 × 2000 CCD plane (16-bit pixel depth) with an exposure of 3 to 20 s. Spatial resolutions (in voxels) were 1.17 to 4.59 μm, depending on the size of the analyzed fragment, and beam hardening was corrected for the XCT images with a constant value of 0.05.

To conduct petrofabric measurements, the data were loaded into the Avizo software, and a nonlocal means filter was applied to reduce noise in the images. Nonlocal means filter parameters were as follows: search window −9, local neighbor −4, and similarity value −0.4. Chondrules were identified within the XCT data by a difference in x-ray attenuation when compared to the matrix (i.e., darker appearance) and the presence of FGRs. Following identification, a representative section of each chondrule was manually segmented in each of the three orthogonal planes (*XY*, *XZ*, and *YZ*) using the Avizo manual segmentation draw tool. A fit ellipsoid was fitted to the outer margins of these segmented sections and measured using the Blob3D software. The resulting directional cosine data for the orientation of the long- and short-shape axis of the ellipsoid were then converted into trend and plunge before being plotted on an equal area stereonet using the Stereonet 11 software. A stereonet illustrating chondrule orientation was produced for each visible lithology to determine whether any petrofabrics (e.g., random, planar, and lineation) were present.

To calculate the macroporosity of the Winchcombe meteorite fragments BM.2022,M2-34 (0.24 g) and BM.2022,M3-31 (<0.01 g), the XCT data were loaded into Avizo, and a total of five internal subvolumes were extracted from the dominant lithologies present. The subvolumes were then segmented using a general thresholding technique to approximately extract the macroscale pores and fractures. Following segmentation, a small spot removal function was applied to remove regions of less than five connected voxels in an attempt to reduce noise. Once macroporosity was segmented, a material statistics function was applied to ascertain the number of voxels segmented as pore space.

Thermogravimetric analysis

Approximately 45 mg of the Winchcombe meteorite powder BM.2022,M1-88 was characterized on 5 March 2021 using a TA Instruments Simultaneous Thermal Analysis (SDT) Q600 at the NHM. The powder was loaded into an alumina crucible and placed onto the TGA balance within a furnace that was then sealed. The mass of the sample was recorded as it was heated from ~15° to 1000°C at 10°C min^{-1} under a N_2 flow of 100 ml min^{-1}. The sensitivity of the TGA balance is 0.1 μg, and the overall error on the measured mass loss fractions is ~0.1% (*60*).

Previous studies of hydrated carbonaceous chondrites have divided TGA curves into distinct temperature regions: (i) mass loss at <100°C is attributed to the removal of adsorbed terrestrial water; (ii) from 100° to 200°C mainly to the breakdown of sulfates; (iii) between 200° and 400°C and 400° and 770°C due to the release of -OH/H_2O in Fe-(oxy)hydroxides and phyllosilicates, respectively; and (iv) between 770° and 900°C from CO_2 produced during the breakdown of carbonates (*60*, *61*). Additional mass loss in these temperature ranges could also result from the decomposition of Fe-sulfides and refractory organic matter, although the contribution is expected to be small.

Hydrogen pyrolysis

The abundance and isotopic composition of hydrogen in the Winchcombe meteorite was analyzed by stepwise pyrolysis at the Scottish Universities Environmental Research Centre (SUERC). Two chips (BM.2022,M2-39, which split into two chips during transport) sealed in glass vials on 16 March 2021 were transferred to a desiccator on 18 March 2021. The smaller chip (BM.2022,M2-39-a, 45.1 mg) was put under vacuum on 19 March 2021 before analysis on 23 and 24 March 2021. The other chip was put under vacuum on 24 March and subsequently split into two subsamples: BM.2022,M2-39-b (32.7 mg) and BM.2022,M2-39-c (30.9 mg). Sample BM.2022,M2-39-b was analyzed on 26 March 2021 and BM.2022,M2-39-c on 30 March 2021.

Chips rather than powders were analyzed to minimize the potential for terrestrial contamination (*25*). Each chip was placed in a previously outgassed (to 1100°C) Pt crucible within an all-glass vacuum line, pumped down overnight, and then incrementally heated via a temperature-controlled resistance furnace (25° to 700°C) and temperature-controlled induction furnace (>700°C) over seven steps: 100°, 200°, 300°, 400°, 500°, 700°, and 1100°C (± 5°C). The samples were held at each temperature for at least 30 min. Released gases were first stored in a cold trap at −196°C using a liquid N_2 bath, which was then replaced by a mixture of dry ice and acetone at −78°C, trapping water but releasing other gases. The yield of gas that was not trapped at −78°C was measured using an Edwards PR10-C Pirani vacuum pressure gauge. The dry ice and acetone bath was then removed from the cold trap, which was gently heated to release the water. This water was released to H_2 by exposure to Cr powder at 850°C (*62*). The yield of hydrogen in each step was measured using the Pirani vacuum pressure gauge, and H_2 was collected with a mercury Toepler pump into a small borosilicate vessel with Teflon-sealed high-vacuum valves. The vessels were immediately taken to a VGI Optima mass spectrometer for hydrogen isotope analysis. In-run repeat analyses of water standards (international standards GISP and V-SMOW and internal standard LT-STD) gave a reproducibility of better than ±2‰ for δD.

Carbon and nitrogen pyrolysis

Small chips of Winchcombe meteorite samples BM.2022,M1-85 (5.0502 mg) and BM.2022,M1-86 (5.0981 mg) were analyzed at the Open University using the Finesse system, which can simultaneously measure the abundance and isotopic compositions of He, Ne, Ar, Xe, N, and C [e.g., (*63*, *64*)]. Gases are released by heating the sample in a double-vacuum furnace in which a quartz glass inner tube is separated from the outer corundum tube by an evacuated space.

For analysis of the Winchcombe meteorite, each chip was loaded into a Pt foil (25-mm-thick) capsule and dropped into the extraction furnace through a gate vale and then heated at ~100°C for 0.5 hours under pumping to decrease atmospheric contamination. The samples were analyzed using a high-resolution temperature program of 25°C steps from 100° to 600°C, the temperature range over which most of the carbonaceous matter combusted. Temperature steps of 50° or 100°C were used at higher temperatures as the amount of combustion products decreased. Released gases were separated into fractions [(CO_2 + Xe), (He + Ne), and (N_2 + Ar)] using a combination of cold fingers, molecular sieves, and getters [e.g., (*63*, *64*)]. All the volumes of the vacuum system are calibrated, so the proportion of the total amount of a gas included in one or another fraction is precisely known. The amount of CO_2 was determined by pressure measurement using a Baratron capacitance monometer to a precision of better than ±1%.

The system has magnetic sector mass spectrometers, each equipped with three collectors set for masses [mass/charge ratio (m/z)] of 28, 29, and 30 (for N_2) and 44, 45, and 46 (for CO_2). A single measurement lasted ~1 min, during which ~300 data points were collected for each isotope, providing a precision of 0.3 to 0.5‰. Calculation of $\delta^{13}C$ and $\delta^{15}N$ values was achieved through analysis under identical conditions of appropriate standards measured alternately with the samples [e.g., (*63*, *64*)]. The laboratory standards were calibrated using National Bureau of Standards (NBS) standard calcite (for CO_2) and air (for noble gases and N_2).

The system blank was determined before analysis of the Winchcombe meteorite by stepped combustion of an empty Pt foil capsule over the same temperature range as the sample. The contribution from the system blank at temperatures below 600°C was negligible for C and N and not more than 10% for the noble gases. Above 600°C, correction for system blank becomes more notable as the amount of gas released from the sample decreases. However, the gas-rich nature of the Winchcombe meteorite ensured that even at the highest temperatures, the contribution from the blank was less than about 20% of the released nitrogen and noble gases and 5% of the CO_2.

Selected ion flow tube–mass spectrometry

The profile of C_1 to C_6 alcohols, aldehydes, ketones, and carboxylic acids present in Winchcombe meteorite samples BM.2022,M1-85 (17.8 mg) and BM.2022,M1-86 (15.7 mg) were determined within 10 months of collection. The chips were placed into 20-ml cleaned glass vials, with the headspace flushed with dry nitrogen. Volatile species were then analyzed using selected ion flow tube–mass spectrometry (SIFT-MS) at Anatune Ltd., Cambridge, UK, following their release into the vial headspace, after heating to 150°C for 15 min. An empty vial was processed in the same way to act as a blank.

Low-voltage SEM-EDS

On 11 March 2021, 17 fragments (~0.5 to 8 mm in size, from site 1) of the Winchcombe meteorite were mounted using cleaned stainless-steel tweezers onto carbon-based electrically conductive, double-sided adhesive discs, also known as Leit tabs, stuck to the flat surface of two aluminum SEM pin stubs. The uncoated and unpolished fragments were then quickly transferred to an FEI Quanta 650 FE-SEM at the IAC of the NHM.

The FE-SEM is equipped with a Bruker Quantax EDS system with a high-sensitivity, annular, four-channel Bruker FlatQUAD SDD inserted between the pole piece and sample within the main chamber of the SEM. The annular geometry allows sufficient data collection on uncoated, beam-sensitive, and nonconductive samples with substantial surface topography using ultralow beam currents under high vacuum (*65*). An accelerating voltage of 6 and 9 kV and a beam current of 30 to 190 pA were used, resulting in an input count rate up to 55 kcps. Several of the fragments were initially mapped at 3- and 4-μm pixel resolution using automated stage control to identify features of interest, which were then further analyzed at a pixel resolution down to 16 nm. Follow-up SEM imaging of the features of interest was carried out in the variable pressure mode of the SEM using a low-vacuum cone.

Liquid chromatography–mass spectrometry

Samples

The Winchcombe stones BM.2022,M2-23 and BM.2022,M9-4 were crushed using an agate pestle and mortar to a grain size of <0.1 mm, with six ~50-mg aliquots then taken from each powder. For both samples, three of the aliquots were initially analyzed using untargeted LC-MS, and three were subsequently analyzed using targeted LC-MS (*66*). Six ~50-mg environmental soil controls from sites 1 and 6 (table S4) were also analyzed to identify terrestrial organic molecules in both locations. Figure S25 summarizes the samples and analytical workflow.

Solvent extractions

All samples and environmental controls were crushed using an agate mortar and pestle at SUERC. The mortar and pestle were cleaned with 2% DECON solution, followed by ultrapure water, then acetone, and dried in a positive pressure fume hood environment in between uses.

Solvent extractions were all performed in a positive pressure fume hood. Glassware and metal tools were wrapped in foil and placed in a furnace overnight at 450°C. All glassware, ceramics, and tools were then washed in 2% DECON clean solution and rinsed with ultrapure water and acetone in between uses for different samples. After crushing, three ~50-mg replicates from each powder were weighed out and placed in new sterile Polytetrafluoroethylene (PTFE) screw-top vials. Three procedural blanks (new empty vials opened at that stage) were added at each step of the extraction to pick up any contaminants in the laboratory, starting at the crushing step, with blanks introduced for each new solvent, as well as the pooling and filtering step.

Solvent extractions were performed by adding 1 ml of each solvent to each powdered sample using a Gilson pipette (with a new sterile tip each time) and mixing using a vortex for 10 min at room temperature. Hexane was the first solvent added and mixed, then dichloromethane (DCM), and finally methanol. These solvents were used to target a broad range of apolar to moderately polar molecules. Each solvent was added, mixed, removed, and then placed in a new vial, using fresh pipette tips before the next solvent was added. A total of 330 μl of each solvent extract was then pooled and mixed in a fresh vial to make up a 990-μl extract, which was then removed using a hypodermic needle and syringe (with needles rinsed with a 1:1:1 sterile solvent mixture between uses, and a fresh needle used every five samples), and finally filtered using a 0.45-μm filter, leaving behind ~80 μl, which was placed in a fresh vial, ready for LC-MS analysis.

These pooled and filtered extracts were frozen in PTFE screw-top vials at ~−10°C until LC-MS analysis. Three procedural blanks (fresh vials with solvent added only from that step onward) were added at each new extraction step to identify the introduction of any laboratory contaminants.

Liquid chromatography–mass spectrometry

Hydrophilic interaction liquid chromatography (pHILIC) was carried out on a Dionex UltraMate 3000 RSLC system using a ZIC-pHILIC column (150 mm by 4.6 mm, 5-mm column, Merck Sequant) at the Polyomics Facility, University of Glasgow. The column was maintained at 25°C, and samples were eluted with a linear gradient (20 mM ammonium carbonate in water, A and acetonitrile, B) over 26 min at a flow rate of 0.3 ml min^{-1} (table S22).

The injection volume was 10 μl, and samples were maintained at 5°C before injection. A Thermo Fisher Scientific Orbitrap QExactive was operated in polarity switching mode, and the MS settings were as follows: resolution, 70,000; automatic gain control (AGC), 1×10^6; *m*/*z* range, 70 to 1050; sheath gas, 40; auxiliary gas, 5; sweep gas, 1; probe temperature, 150°C; capillary temperature, 320°C.

For positive-mode ionization, the source voltage was +3.8 kV, S-Lens RF level was 30.00, S-Lens voltage was 25.00 V, skimmer voltage was 15.00 V, inject flatopole offset was 8.00 V, and bent flatopole DC was 6.00 V. For negative-mode ionization, the source voltage was −3.8 kV. The calibration mass range was extended to cover small metabolites by inclusion of low-mass calibrants with the standard Thermo Fisher Scientific calmix masses (below *m*/*z* 138), butylamine ($C_4H_{11}N$) for positive ion electrospray ionization (PIESI) mode (*m*/*z* 74.096426) and COF3 for negative ion electrospray ionization (NIESI) mode (*m*/*z* 84.9906726). To enhance calibration stability, lock-mass correction was also applied to each analytical run: positive-mode lock masses: number of lock masses: 1 lock mass #1 (*m*/*z*): 144.9822; negative-mode lock masses: number of lock masses: 1 lock mass #1 (*m*/*z*): 100.9856.

Instrument .raw files were converted to positive and negative ionization mode mzXML files. These files were processed with IDEOM (*67*), which uses the XCMS (*68*) and mzMatch (*69*) software in the R environment. Briefly, this involves using the CentWare algorithm within XCMS to pick out signals based on their retention time and mass-to-charge ratio. These signals are then grouped on the basis of sample replicates and filtered using relative SD, minimum intensity, and a noise filter to produce a set of signals that are likely to be due to real metabolites.

Last, a gap-filling step was used to ensure that signals that may have been missed or lost from a particular group/groups while retained for another group were reinstated to avoid erroneous identification of signals unique to a particular sample. Fragmentation data were analyzed in PiMP (*70*) with the FrAnK in-house fragmentation data analysis software. Comparisons between the overall metabolite distributions of the samples were made using MetaboAnalyst (*71*).

Gas chromatography–mass spectrometry

Samples, chemicals, and materials

GC-MS was used to characterize the amino acid content of a Winchcombe meteorite stone (BM.2022,M2-14) and nearby soil sample (the "fall site soil"). A powdered sample of serpentinized peridotite from Kennack Sands, UK, was also analyzed as a procedural blank. The procedural blank was heated to 500°C in air for 24 hours before the amino acid extraction procedures. Stock solutions (10^{-3} to 10^{-1} M) of individual amino acids were made by dissolution of standard crystals in ultrapure water. An amino acid standard mixture was made by combining individual standard solutions. The amino acid standard mixture, procedural blank, and fall site soil were subjected to the same experimental procedures as the meteorite sample.

All tools, glassware, and ceramics were sterilized by baking at 500°C in air for 24 hours. Millipore ultrapure water (18.2 megohm·cm, ≤3 parts per billion of total organic carbon) was used for all laboratory work performed in this study. The amino acid 3-amino-3-methyl butanoic acid and 3-amino-2,2-dimethylpropanoic acid were provided by the Astrobiology Analytical Laboratory at Goddard Space Flight Center, NASA. All other amino acid standard crystals/powder were purchased from Acros Organics, Sigma-Aldrich, and Fluka. Hydrochloric acid (HCl; 37%), ammonium hydroxide (NH_4OH) (28 to 30 wt %), isopropanol (IPA; 99.5%), and trifluoroacetic anhydride (TFAA; >99.0%) were purchased from Sigma-Aldrich. Acetyl chloride (99+%) and pyrene (98%) were from Acros Organics. Prepacked columns, analytical grade 50W-X8, hydrogen form (100 to 200 mesh) were acquired from Bio-Rad. Sodium hydroxide (NaOH) pellets and DCM (99.8+%) were purchased from Fisher Scientific.

Sample extraction and desalting procedures

The Winchcombe meteorite sample was powdered, split into five equal portions, and transferred to individual test tubes (20 × 150 mm) for hot-water extraction. Ultrapure water (1 ml) was added to each sample. The test tubes were then flame-sealed and heated to 100°C for 24 hours in a heating block. After cooling to room temperature, the test tubes were rinsed with ultrapure water, cracked open, and centrifuged for 5 min. Eighty percent of the water supernatant was transferred to small test tubes (12 × 75 mm) individually, dried under vacuum, flame-sealed in a larger test tube (20 × 150 mm) containing 1 ml of 6 N HCl, and then subjected to acid vapor hydrolysis for 3 hours at 150°C to determine the total (free + bound) amino acid content. Fifteen percent of the water supernatant (the nonhydrolyzed fraction) was transferred to small test tubes and kept in a fridge until before the desalting procedure. After the hydrolysis procedure, the test tubes were rinsed with ultrapure water and then cracked open. The small test tubes were removed and dried under vacuum.

Cation exchange was performed on prepacked columns. The columns were prepared according to the following procedures. After removing the caps and snapping off the seals on the Luer tips, the columns were filled to the top with water (~10 ml) plus one bed volume (~2 ml). Once the volume of water was just above the resin bed, three bed volumes (~6 ml) of 2 M NaOH was added to desorb any contaminating amino acids. The columns were then washed by filling to the top with water twice (20 ml) until the eluting solution had a neutral pH to remove residual NaOH. Three bed volumes (~6 ml) of 1.5 M HCl was added to re-acidify the columns. The columns were again washed with two volumes of water (20 ml) to remove excess HCl until neutral pH.

Both hydrolyzed and nonhydrolyzed samples were then brought up in 3 × 1 ml of ultrapure water and desalted on the cation exchange resin. Different fractions of the same sample were recombined by desalting in the same column. Purified amino acids were eluted by adding 2 × 3.5-ml fractions of 2 M NH_4OH, and the eluates were collected in small test tubes, which were then evaporated to dryness by vacuum centrifugation.

TFAA-IPA derivatization and GC-MS analysis

Before GC-MS analysis, amino acids were derivatized by esterification with IPA and acylation with TFAA. The samples were resuspended in 2 × 50 μl of ultrapure water in inserts within GC vials. A total of 100 μl of acetyl chloride:IPA mixture (30:70, v/v) was added to each of the samples. The vials were tightly capped, and the samples were heated in a heating block set at 110°C for 1 hour. The samples were then cooled in an ice bath and dried under a gentle stream of dry N_2. After the samples were brought to room temperature, 100 μl of DCM and 50 μl of TFAA were added to the dried sample. The vials were capped tightly again and heated to 100°C for 10 min. The samples were then cooled to room temperature, and the excess reagent was removed under a slow stream of N_2. Before injection, the derivatized samples were dissolved in 30 μl of DCM and 5 μl of pyrene in DCM (200 μg/ml) as an internal standard. The derivatized samples were then immediately analyzed by GC-MS.

Amino acids in the hot water extracts were analyzed by an Agilent Technologies 7890A series GC coupled to an Agilent Technologies 5975C mass-selective detector (MSD). The separations of the D,L-amino acid enantiomers were achieved using a CP-Chirasil-L Val GC column [25 m × 0.25 mm inside diameter (ID) × 0.12 μm; Agilent Technologies]. For separation of the D,L-isovaline enantiomers, a 6890N series GC coupled to a 5973 MSD (both Agilent Technologies) and a CP-Chirasil-Dex CB GC column (25 m × 0.25 mm ID × 0.25 μm; Agilent Technologies) were used.

Helium was used as the carrier gas, the column flow rate was set at 1.1 ml min^{-1}, and injection (1 μl) was in split mode (10:1) at 220°C. The source and quadrupole temperatures were maintained at 230° and 150°C, respectively, and the MSD transfer line was heated to 180°C. Standard autotunes with perfluorotributylamine and air/water checks were made daily. The oven program was set at an initial temperature of 90°C and held for 2 min, then increased by 5°C min^{-1} to 200°C, and held for 6 min. GC-MS methods were the same for both instruments used. Total ion current chromatograms were acquired and analyzed with the Agilent Technologies MSD ChemStation (6890-5973) or MassHunter (7890-5975) software packages. Amino acids present in the Winchcombe meteorite samples were identified by comparison of the retention time and mass fragmentation pattern with a known amino acid standard reference mixture, and quantification was made by chromatographic data collected in the selected ion monitoring mode. Identification was added by retention time locking of the GC method and creation of a custom library from standards that include retention time and retention indices for the amino acids.

Supplementary Materials

This PDF file includes:

Supplementary Materials and Methods
Figs. S1 to S26
Tables S1 to S23
References

REFERENCES AND NOTES

1. T. S. Kruijer, C. Burkhardt, G. Budde, T. Kleine, Age of Jupiter inferred from the distinct genetics and formation times of meteorites. *Proc. Natl. Acad. Sci. U.S.A.* **114**, 6712–6716 (2017).
2. T. Lichtenberg, J. Drążkowska, M. Schöbächler, G. J. Golabek, T. O. Hands, Bifurcation of planetary building blocks during solar system formation. *Science* **371**, 365–370 (2021).
3. K. J. Walsh, A. Morbidelli, S. N. Raymond, D. P. O'Brien, A. M. Mandell, Populating the asteroid belt from two parent source regions due to the migration of giant planets—"The Grand Tack". *Meteorit. Planet. Sci.* **47**, 1941–1947 (2012).
4. F. E. DeMeo, B. Carry, Solar system evolution from compositional mapping of the asteroid belt. *Nature* **505**, 629–634 (2014).
5. C. M. O'. D. Alexander, R. Bowden, M. L. Fogel, K. T. Howard, C. D. K. Herd, L. R. Nittler, The provenances of asteroids, and their contributions to the volatile inventories of the terrestrial planets. *Science* **337**, 721–723 (2012).
6. P. G. Brown, A. R. Hildebrand, M. E. Zolensky, M. Grady, R. N. Clayton, T. K. Mayeda, E. Tagliaferri, R. Spalding, N. D. MacRae, E. L. Hoffman, D. W. Mittlefehldt, J. F. Wacker, J. A. Bird, M. D. Campbell, R. Carpenter, H. Gingerich, M. Glatiotis, E. Greiner, M. J. Mazur, P. J. A. McCausland, H. Plotkin, T. R. Mazur, The fall, recovery, orbit, and composition of the Tagish Lake meteorite: A new type of carbonaceous chondrite. *Science* **290**, 320–325 (2000).
7. P. Jenniskens, M. D. Fries, Q.-Z. Yin, M. Zolensky, A. N. Krot, S. A. Sandford, D. Sears, R. Beauford, D. S. Ebel, J. M. Friedrich, K. Nagashima, J. Wimpenny, A. Yamakawa, K. Nishiizumi, Y. Hamajima, M. W. Caffee, K. C. Welten, M. Laubenstein, A. M. Davis, S. B. Simon, P. R. Heck, E. D. Young, I. E. Kohl, M. H. Thiemens, M. H. Nunn, T. Mikouchi, K. Hagiya, K. Ohsumi, T. A. Cahill, J. A. Lawton, D. Barnes, A. Steele, P. Rochette, K. L. Verosub, J. Gattacceca, G. Cooper, D. P. Glavin, A. S. Burton, J. P. Dworkin, J. E. Elsila, S. Pizzarello, R. Ogliore, P. Schmitt-Kopplin, M. Harir, N. Hertkorn, A. Verchovsky, M. Grady, K. Nagao, R. Okazaki, H. Takechi, T. Hiroi, K. Smith, E. A. Silber, P. G. Brown, J. Albers, D. Klotz, M. Hankey, R. Matson, J. A. Fries, R. J. Walker, I. Puchtel, C.-T. A. Lee, M. E. Erdman, G. R. Eppich, S. Roeske, Z. Gabelica, M. Lerche, M. Nuevo, B. Girten, S. P. Worden, Radar-enabled recovery of the Sutter's Mill meteorite, a carbonaceous chondrite regolith breccia. *Science* **338**, 1583–1587 (2012).
8. J. Borovička, O. Popova, P. Spurný, The Maribo CM2 meteorite fall—Survival of weak material at high entry speed. *Meteorit. Planet. Sci.* **54**, 1024–1041 (2019).
9. J. Borovička, F. Bettonvil, G. Baumgarten, J. Strunk, M. Hankey, P. Spurný, D. Heinlein, Trajectory and orbit of the unique carbonaceous meteorite Flensburg. *Meteorit. Planet. Sci.* **56**, 425–439 (2021).
10. W. F. Bottke, D. Vokrouhlický, K. J. Walsh, M. Delbo, P. Michel, D. S. Lauretta, H. Campins, H. C. Connolly Jr., D. J. Scheeres, S. R. Chelsey, In search of the source of asteroid (101955) Bennu: Applications of the stochastic YORP model. *Icarus* **247**, 191–217 (2015).
11. T. Morota, S. Sugita, Y. Cho, M. Kanamaru, E. Tatsumi, N. Sakatani, R. Honda, N. Hirata, H. Kikuchi, M. Yamada, Y. Yokota, S. Kameda, M. Matsuoka, H. Sawada, C. Honda, T. Kouyama, K. Ogawa, H. Suzuki, K. Yoshioka, M. Hayakawa, N. Hirata, M. Hirabayashi, H. Miyamoto, T. Michikami, T. Hiroi, R. Hemmi, O. S. Barnouin, C. M. Ernst, K. Kitazato, T. Nakamura, L. Riu, H. Senshu, H. Kobayashi, S. Sasaki, G. Komatsu, N. Tanabe, Y. Fujii, T. Irie, M. Suemitsu, N. Takaki, C. Sugimoto, K. Yumoto, M. Ishida, H. Kato, K. Moroi, D. Domingue, P. Michel, C. Pilorget, T. Iwata, M. Abe, M. Ohtake, Y. Nakauchi, K. Tsumura, H. Yabuta, Y. Ishihara, R. Noguchi, K. Matsumoto, A. Miura, N. Namiki, S. Tachibana, M. Arakawa, H. Ikeda, K. Wada, T. Mizuno, C. Hirose, S. Hosoda, O. Mori, T. Shimada, S. Soldini, R. Tsukizaki, H. Yano, M. Ozaki, H. Takeuchi, Y. Yamamoto, T. Okada, Y. Shimaki, K. Shirai, Y. Iijima, H. Noda, S. Kikuchi, T. Yamaguchi, N. Ogawa, G. Ono, Y. Mimasu, K. Yoshikawa, T. Takahashi, Y. Takei, A. Fujii, S. Nakazawa, F. Terui, S. Tanaka, M. Yoshikawa, T. Saiki, S. Watanabe, Y. Tsuda, Sample collection from asteroid (162173) Ryugu by Hayabusa2: Implications for surface evolution. *Science* **368**, 654–659 (2020).
12. M. Granvik, P. Brown, Identification of meteorite source regions in the solar system. *Icarus* **311**, 271–287 (2018).
13. P. M. Schober, E. K. Sansom, P. A. Bland, H. A. R. Devillepoix, M. C. Towner, M. Cupák, R. M. Howie, B. A. D. Hartig, S. L. Anderson, The main asteroid belt: The primary source of debris on comet-like orbits. *Planet. Sci.* **2**, 98 (2021).
14. P. Farinella, D. Vokrouhlický, W. K. Hartmann, Meteorite delivery via Yarkovsky orbital drift. *Icarus* **132**, 378–387 (1998).
15. D. Krietsch, H. Busemann, M. E. I. Riebe, A. J. King, C. M. O'. D. Alexander, C. Maden, Noble gases in CM carbonaceous chondrites: Effect of parent body aqueous and thermal alteration and cosmic ray exposure ages. *Geochim. Cosmochim. Acta* **310**, 240–280 (2021).
16. J. Borovička, P. Spurný, L. Shrbený, Two strengths of ordinary chondritic meteoroids as derived from their atmospheric fragmentation modeling. *Astronom. J.* **160**, 42 (2020).
17. R. N. Clayton, T. K. Mayeda, Oxygen isotope studies of carbonaceous chondrites. *Geochim. Cosmochim. Acta* **63**, 2089–2104 (1999).
18. D. L. Schrader, I. A. Franchi, H. C. Connolly Jr., R. C. Greenwood, D. S. Lauretta, J. M. Gibson, The formation and alteration of the Renazzo-like carbonaceous chondrites I: Implications of bulk-oxygen isotopic composition. *Geochim. Cosmochim. Acta* **75**, 308–325 (2011).
19. E. Tonui, M. Zolensky, T. Hiroi, T. Nakamura, M. E. Lipschutz, M.-S. Wang, K. Okudaira, Petrographic, chemical and spectroscopic evidence for thermal metamorphism in carbonaceous chondrites I: CI and CM chondrites. *Geochim. Cosmochim. Acta* **126**, 284–306 (2014).
20. K. Tomeoka, P. R. Buseck, Indicators of aqueous alteration in CM carbonaceous chondrites: Microtextures of a layered mineral containing Fe, S, O and Ni. *Geochim. Cosmochim. Acta* **49**, 2149–2163 (1985).
21. A. E. Rubin, J. M. Trigo-Rodríguez, H. Huber, J. T. Wasson, Progressive aqueous alteration of CM carbonaceous chondrites. *Geochim. Cosmochim. Acta* **71**, 2361–2382 (2007).
22. P. Michel, R.-L. Ballouz, O. S. Barnouin, M. Jutzi, K. J. Walsh, B. H. May, C. Manzoni, D. C. Richardson, S. R. Schwartz, S. Sugita, S. Watanabe, H. Miyamoto, M. Hirabayashi, W. F. Bottke, H. C. Connolly, M. Yoshikawa, D. S. Lauretta, Collisional formation of top-shaped asteroids and implications for the origins of Ryugu and Bennu. *Nat. Commun.* **11**, 2655 (2020).
23. C. M. O'. D. Alexander, K. T. Howard, R. Bowden, M. L. Fogel, The classification of CM and CR chondrites using bulk H, C and N abundances and isotopic compositions. *Geochim. Cosmochim. Acta* **123**, 244–260 (2013).
24. L. G. Vacher, L. Piani, T. Rigaudier, D. Thomassin, G. Florin, M. Piralla, Y. Marrocchi, Hydrogen in chondrites: Influence of parent body alteration and atmospheric contamination on primordial components. *Geochim. Cosmochim. Acta* **281**, 53–66 (2020).
25. M. R. Lee, B. E. Cohen, A. J. Boyce, L. J. Hallis, L. Daly, The pre-atmospheric hydrogen inventory of CM carbonaceous chondrites. *Geochim. Cosmochim. Acta* **309**, 31–44 (2021).
26. M. R. Lee, L. Daly, C. Floyd, P.-E. Martin, CM carbonaceous chondrite falls and their terrestrial alteration. *Meteorit. Planet. Sci.* **56**, 34–48 (2021).
27. E. T. Peltzer, J. L. Bada, G. Schlesinger, S. L. Miller, The chemical conditions on the parent body of the Murchison meteorite: Some conclusions based on amino, hydroxy and dicarboxylic acids. *Adv. Space Res.* **4**, 69–74 (1984).
28. O. Botta, Z. Martins, P. Ehrenfreund, Amino acids in Antarctic CM1 meteorites and their relationship to other carbonaceous chondrites. *Meteorit. Planet. Sci.* **42**, 81–92 (2007).
29. D. P. Glavin, M. P. Callahan, J. P. Dworkin, J. E. Elsila, The effects of parent body processes on amino acids in carbonaceous chondrites. *Meteorit. Planet. Sci.* **45**, 1948–1972 (2011).
30. J. R. Cronin, S. Pizzarello, Enantiomeric excesses in meteoritic amino acids. *Science* **275**, 951–955 (1997).
31. D. P. Glavin, J. E. Elsila, H. L. Mclain, J. C. Aponte, E. T. Parker, J. P. Dworkin, D. H. Hill, H. C. Connolly Jr., D. S. Lauretta, Extraterrestrial amino acids and L-enantiomeric excesses in the CM2 carbonaceous chondrites Aguas Zarcas and Murchison. *Meteorit. Planet. Sci.* **56**, 148–173 (2021).
32. H. A. R. Devillepoix, M. Cupák, P. A. Bland, E. K. Sansom, M. C. Towner, R. M. Howie, B. A. D. Hartig, T. Jansen-Sturgeon, P. M. Shober, S. L. Anderson, G. K. Benedix, A global fireball observatory. *Planet. Space Sci.* **191**, 105036 (2020).
33. F. Colas, B. Zanda, S. Bouley, S. Jeanne, A. Malgoyre, M. Birlan, C. Blanpain, J. Gattacceca, L. Jorda, J. Lecubin, C. Marmo, J. L. Rault, J. Vaubaillon, P. Vernazza, C. Yohia, D. Gardiol, A. Nedelcu, B. Poppe, J. Rowe, M. Forcier, D. Koschny, J. M. Trigo-Rodriguez, H. Lamy, R. Behrend, L. Ferrière, D. Barghini, A. Buzzoni, A. Carbognani, M. di Carlo, M. di Martino, C. Knapic, E. Londero, G. Pratesi, S. Rasetti, W. Riva, G. M. Stirpe, G. B. Valsecchi, C. A. Volpicelli, S. Zorba, D. Coward, E. Drolshagen, G. Drolshagen, O. Hernandez, E. Jehin, M. Jobin, A. King, C. Nitschelm, T. Ott, A. Sanchez-Lavega, A. Toni, P. Abraham, F. Affaticati, M. Albani, A. Andreis, T. Andrieu, S. Anghel, E. Antaluca, K. Antier, T. Appéré, A. Armand, G. Ascione, Y. Audureau, G. Auxepaules, T. Avoscan, D. B. Aissa, P. Bacci, O. Bădescu, R. Baldini, R. Baldo, A. Balestrero, D. Baratoux, E. Barbotin, M. Bardy, S. Basso, O. Bautista, L. D. Bayle, P. Beck, R. Bellitto, R. Belluso, C. Benna, M. Benammi, E. Beneteau, Z. Benkhaldoun, P. Bergamini, F. Bernardi, M. E. Bertaina, P. Bessin, L. Betti, F. Bettonvil, D. Bihel, C. Birnbaum, O. Blagoi, E. Blouri, I. Boacă, R. Boată, B. Bobiet, R. Bonino, K. Boros, E. Bouchet, V. Borgeot, E. Bouchez, D. Boust, V. Boudon, T. Bouman, P. Bourget, S. Brandenburg, P. Bramond, E. Braun, A. Bussi, P. Cacault, B. Caillier, A. Calegaro, J. Camargo, S. Caminade, A. P. C. Campana, P. Campbell-Burns, R. Canal-Domingo, O. Carell, S. Carreau, E. Cascone, C. Cattaneo, P. Cauhape, P. Cavier, S. Celestin, A. Cellino, M. Champenois, H. C. Aoudjehane, S. Chevrier, P. Cholvy, L. Chomier, A. Christou, D. Cricchio, P. Coadou, J. Y. Cocaign, F. Cochard, S. Cointin, E. Colombi, J. P. C. Saavedra, L. Corp, M. Costa, F. Costard, M. Cottier, P. Cournoyer, E. Coustal, G. Cremonese, O. Cristea,

J. C. Cuzon, G. D'Agostino, K. Daiffallah, C. Dănescu, A. Dardon, T. Dasse, C. Davadan, V. Debs, J. P. Defaix, F. Deleflie, M. D'Elia, P. de Luca, P. de Maria, P. Deverchère, H. Devillepoix, A. Dias, A. di Dato, R. di Luca, F. M. Dominici, A. Drouard, J. L. Dumont, P. Dupouy, L. Duvignac, A. Egal, N. Erasmus, N. Esseiva, A. Ebel, B. Eisengarten, F. Federici, S. Feral, G. Ferrant, E. Ferreol, P. Finitzer, A. Foucault, P. Francois, M. Frîncu, J. L. Froger, F. Gaborit, V. Gagliarducci, J. Galard, A. Gardavot, M. Garmier, M. Garnung, B. Gautier, B. Gendre, D. Gerard, A. Gerardi, J. P. Godet, A. Grandchamps, B. Grouiez, S. Groult, D. Guidetti, G. Giuli, Y. Hello, X. Henry, G. Herbreteau, M. Herpin, P. Hewins, J. J. Hillairet, J. Horak, R. Hueso, E. Huet, S. Huet, F. Hyaumé, G. Interrante, Y. Isselin, Y. Jeangeorges, P. Janeux, P. Jeanneret, K. Jobse, S. Jouin, J. M. Jouvard, K. Joy, J. F. Julien, R. Kacerek, M. Kaire, M. Kempf, D. Koschny, C. Krier, M. K. Kwon, L. Lacassagne, D. Lachat, A. Lagain, E. Laisné, V. Lanchares, J. Laskar, M. Lazzarin, M. Leblanc, J. P. Lebreton, J. Lecomte, P. le Dû, F. Lelong, S. Lera, J. F. Leoni, A. le-Pichon, P. le-Poupon, A. Leroy, G. Leto, A. Levansuu, E. Lewin, A. Lienard, D. Licchelli, H. Locatelli, S. Loehle, D. Loizeau, L. Luciani, M. Maignan, F. Manca, S. Mancuso, E. Mandon, N. Mangold, F. Mannucci, L. Maquet, D. Marant, Y. Marchal, J. L. Marin, J. C. Martin-Brisset, D. Martin, D. Mathieu, A. Maury, N. Mespoulet, F. Meyer, J. Y. Meyer, E. Meza, V. M. Cecchi, J. J. Moiroud, M. Millan, M. Montesarchio, A. Misiano, E. Molinari, S. Molau, J. Monari, B. Monflier, A. Monkos, M. Montemaggi, G. Monti, R. Moreau, J. Morin, R. Mourgues, O. Mousis, C. Nablanc, A. Nastasi, L. Niacşu, P. Notez, M. Ory, E. Pace, M. A. Paganelli, A. Pagola, M. Pajuelo, J. F. Palacián, G. Pallier, P. Paraschiv, R. Pardini, M. Pavone, G. Pavy, G. Payen, A. Pegoraro, E. Peña-Asensio, L. Perez, S. Pérez-Hoyos, V. Perlerin, A. Peyrot, F. Peth, V. Pic, S. Pietronave, C. Pilger, M. Piquel, T. Pisanu, M. Poppe, L. Portois, J. F. Prezeau, N. Pugno, C. Quantin, G. Quitté, N. Rambaux, E. Ravier, U. Repetti, S. Ribas, C. Richard, D. Richard, M. Rigoni, J. P. Rivet, N. Rizzi, S. Rochain, J. F. Rojas, M. Romeo, M. Rotaru, M. Rotger, P. Rougier, P. Rousselot, J. Rousset, D. Rousseu, O. Rubiera, R. Rudawska, J. Rudelle, J. P. Ruguet, P. Russo, S. Sales, O. Sauzereau, F. Salvati, M. Schieffer, D. Schreiner, Y. Scribano, D. Selvestrel, R. Serra, L. Shengold, A. Shuttleworth, R. Smareglia, S. Sohy, M. Soldi, R. Stanga, A. Steinhausser, F. Strafella, S. S. Mbaye, A. R. D. Smedley, M. Tagger, P. Tanga, C. Taricco, J. P. Teng, J. O. Tercu, O. Thizy, J. P. Thomas, M. Tombelli, R. Trangosi, B. Tregon, P. Trivero, A. Tukkers, V. Turcu, G. Umbriaco, E. Unda-Sanzana, R. Vairetti, M. Valenzuela, G. Valente, G. Varennes, S. Vauclair, J. Vergne, M. Verlinden, M. Vidal-Alaiz, R. Vieira-Martins, A. Viel, D. C. Vîntdevară, V. Vinogradoff, P. Volpini, M. Wendling, P. Wilhelm, K. Wohlgemuth, P. Yanguas, R. Zagarella, A. Zollo, FRIPON: A worldwide network to track incoming meteoroids. *Astron. Astrophys.* **644**, A53 (2020).

34. D. Vida, D. Šegon, P. S. Gural, P. G. Brown, M. J. McIntyre, T. J. Dijkema, L. Pavletić, P. Kukić, M. J. Mazur, P. Eschman, P. Roggemans, A. Merlak, D. Zubović, The Global Meteor Network—Methodology and first results. *Mon. Notices Royal Astron. Soc.* **506**, 5046–5074 (2021).
35. M. Hankey, V. Perlerin, D. Meisel, The all-sky-6 and the Video Meteor Archive system of the AMS Ltd. *Planet. Space Sci.* **190**, 105005 (2020).
36. T. J. Warren, N. E. Bowles, K. Donaldson Hanna, I. R. Thomas, The Oxford Space Environment Goniometer: A new experimental setup for making directional emissivity measurements under a simulated space environment. *Rev. Sci. Instr.* **88**, 124502 (2017).
37. B. Hapke, Bidirectional reflectance spectroscopy 7: The single particle phase function hockey stick relation. *Icarus* **221**, 1079–1083 (2012).
38. D. Györe, L. Di Nicola, D. Currie, F. M. Stuart, New system for measuring cosmogenic Ne in terrestrial and extra-terrestrial rocks. *Geosci.* **11**, 353 (2021).
39. P. P. Povinec, I. Sýkora, V. Porubčan, M. Ješkovský, Analysis of ^{26}Al in meteorite samples by coincidence gamma-ray spectrometry. *J. Radioanal. Nucl. Chem.* **282**, 805–808 (2009).
40. P. P. Povinec, I. Sýkora, A. Kováčik, C. Koeberl, High-sensitivity HPGe gamma-spectrometry analysis of radionuclides in Martian meteorites. *J. Radioanal. Nucl. Chem.* **307**, 2403–2407 (2016).
41. M. Laubenstein, Screening of materials with high purity germanium detectors at the Laboratori Nazionali del Gran Sasso. *Intern. J. Modern Phys. A* **32**, 1743002 (2017).
42. S. Agostinelli, J. Allison, K. Amako, J. Apostolakis, H. Araujo, P. Arce, M. Asai, D. Axen, S. Banerjee, G. Barrand, F. Behner, L. Bellagamba, J. Boudreau, L. Broglia, A. Brunengo, H. Burkhardt, S. Chauvie, J. Chuma, R. Chytracek, G. Cooperman, G. Cosmo, P. Degtyarenko, A. Dell'Acqua, G. Depaola, D. Dietrich, R. Enami, A. Feliciello, C. Ferguson, H. Fesefeldt, G. Folger, F. Foppiano, A. Forti, S. Garelli, S. Giani, R. Giannitrapani, D. Gibin, J. J. Gómez Cadenas, I. González, G. Gracia Abril, G. Greeniaus, W. Greiner, V. Grichine, A. Grossheim, S. Guatelli, P. Gumplinger, R. Hamatsu, K. Hashimoto, H. Hasui, A. Heikkinen, A. Howard, V. Ivanchenko, A. Johnson, F. W. Jones, J. Kallenbach, N. Kanaya, M. Kawabata, Y. Kawabata, M. Kawaguti, S. Kelner, P. Kent, A. Kimura, T. Kodama, R. Kokoulin, M. Kossov, H. Kurashige, E. Lamanna, T. Lampén, V. Lara, V. Lefebure, F. Lei, M. Liendl, W. Lockman, F. Longo, S. Magni, M. Maire, E. Medernach, K. Minamimoto, P. M. de Freitas, Y. Morita, K. Murakami, M. Nagamatu, R. Nartallo, P. Nieminen, T. Nishimura, K. Ohtsubo, M. Okamura, S. O'Neale, Y. Oohata, K. Paech, J. Perl, A. Pfeiffer, M. G. Pia, F. Ranjard, A. Rybin, S. Sadilov, E. di Salvo, G. Santin, T. Sasaki, N. Savvas, Y. Sawada, S. Scherer, S. Sei, V. Sirotenko, D. Smith, N. Starkov, H. Stoecker, J. Sulkimo, M. Takahata, S. Tanaka, E. Tcherniaev, E. Safai Tehrani, M. Tropeano, P. Truscott, H. Uno, L. Urban, P. Urban, M. Verderi, A. Walkden, W. Wander, H. Weber, J. P. Wellisch, T. Wenaus, D. C. Williams, D. Wright, T. Yamada, H. Yoshida, D. Zschiesche, GEANT 4—A simulation toolkit. *Nucl. Instrum. Meth. Phys. A* **506**, 250–303 (2003).
43. A. J. T. Jull, L. R. McHargue, P. A. Bland, R. C. Greenwood, W. R. Bevan, K. J. Kim, M. D. Giscard, S. E. LaMotta, J. A. Johnson, Terrestrial ages of meteorites from the Nullarbor region, Australia, based on ^{14}C and ^{14}C-^{10}Be measurements. *Meteorit. Planet. Sci.* **45**, 1271–1283 (2010).
44. LNHB, Laboratoire National Henry Becquerel. 2013. Nucleide; www.nucleide.org.
45. M. F. Miller, I. A. Franchi, A. S. Sexton, C. T. Pillinger, High precision Δ^{17}O isotope measurements of oxygen from silicates and other oxides: Method and applications. *Rapid. Commun. Mass Spec.* **13**, 1211–1217 (1999).
46. D. L. Schrader, J. Davidson, R. C. Greenwood, I. A. Franchi, J. M. A. Gibson, A water-ice rich minor body from the early solar system: The CR chondrite parent asteroid. *Earth Planet. Sci. Lett.* **407**, 48–60 (2014).
47. N. A. Starkey, C. R. M. Jackson, R. C. Greenwood, S. Parman, I. A. Franchi, M. Jackson, J. G. Fitton, F. M. Stuart, M. Kurz, L. M. Larsen, Triple oxygen isotopic composition of the high ^{3}He/^{4}He mantle. *Geochim. Cosmochim. Acta* **176**, 227–238 (2016).
48. F. R. Niederer, D. A. Papanastassiou, G. J. Wasserburg, The isotopic composition of titanium in the Allende and Leoville meteorites. *Geochim. Cosmochim. Acta* **45**, 1017–1031 (1981).
49. W. A. Russell, D. A. Papanastassiou, T. A. Tombrello, Ca isotope fractionation on the Earth and other solar system materials. *Geochim. Cosmochim. Acta* **42**, 1075–1090 (1978).
50. G. D. Flesch, J. Capellen, H. J. Svec, *Advanced Mass Spectrometry III*, pp. 571–581, Leiden, London (1996).
51. W. R. Shields, T. J. Murphy, E. J. Catanzaro, E. L. Garner, Absolute isotopic abundance ratios and the atomic weight of a reference sample of chromium. *J. Res. Natl. Bur. Stand. A* **70**, 193–197 (1966).
52. A. Trinquier, J.-L. Birck, C. J. All'egre, High-precision analysis of chromium isotopes in terrestrial and meteorite samples by thermal ionization mass spectrometry. *J. Anal. At. Spectrom.* **23**, 1565–1574 (2008).
53. M. Schiller, E. Van Kooten, J. C. Holst, M. B. Olsen, M. Bizzarro, Precise measurement of chromium isotopes by MC-ICPMS. *JAAS* **29**, 1406–1416 (2014).
54. J. L. Pouchou, F. Pichoir, Quantitative analysis of homogenous or stratified microvolumes applying the model "PAP", in *Electron Probe Quantification*, K. F. J. Heinrich, D. E. Newbury, Eds. (Springer, 1991), pp. 31–75.
55. M. R. Lee, P. A. Bland, G. Graham, Preparation of TEM samples by focused ion beam (FIB) techniques: Applications to the study of clays and phyllosilicates in meteorites. *Min. Mag.* **67**, 581–592 (2003).
56. S. Sridhar, J. F. J. Bryson, A. J. King, R. J. Harrison, Constraints on the ice composition of carbonaceous chondrites from their magnetic mineralogy. *Earth Planet. Sci. Lett.* **576**, 117243 (2021).
57. R. Egli, VARIFORC: An optimized protocol for calculating non-regular first-order reversal curve (FORC) diagrams. *Glob. Planet. Change* **110**, 302–320 (2013).
58. R. Harrison, J. Feinberg, FORCinel: An improved algorithm for calculating first-order reversal curve distributions using locally weighted regression smoothing. *Geochem. Geophys. Geosyst.* **9**, Q05016 (2008).
59. R. Harrison, J. Murszko, D. Heslop, I. Lascu, A. Muxworth, A. Roberts, An improved algorithm for unmixing first-order reversal curve diagrams using principal component analysis. *Geochem. Geophys. Geosyst.* **19**, 1595–1610 (2018).
60. A. J. King, J. R. Solomon, P. F. Schofield, S. S. Russell, Characterising the CI and CI-like carbonaceous chondrites using thermogravimetric analysis and infrared spectroscopy. *Earth Planets Space* **67**, 198 (2015).
61. A. Garenne, P. Beck, G. Montes-Hernandez, R. Chiriac, F. Toche, E. Quirico, L. Bonal, B. Schmitt, The abundance and stability of "water" in type 1 and 2 carbonaceous chondrites (CI, CM and CR). *Geochim. Cosmochim. Acta* **137**, 93–112 (2014).
62. T. Donnelly, S. Waldron, A. Tait, J. Dougans, S. Bearhop, Hydrogen isotope analysis of natural abundance and deuterium-enriched waters by reduction over chromium on-line to a dynamic dual inlet isotope-ratio mass spectrometer. *Rapid Commun. Mass Spectrom.* **15**, 1297–1303 (2001).
63. I. P. Wright, N. J. McNaughton, A. E. Fallick, L. R. Gardiner, C. T. Pillinger, A high-precision mass spectrometer for stable carbon isotope analysis at the nanogram level. *J. Phys. E Sci. Instr.* **16**, 497–504 (1983).
64. I. P. Wright, S. R. Boyd, I. A. Franchi, C. T. Pillinger, High-precision determination of nitrogen stable isotope ratios at the sun-nanomole level. *J. Phys.* **E21**, 865–875 (1988).
65. R. Terborg, A. Kaeppel, B. Yu, M. Patzschke, T. Salge, M. Falke, Advanced chemical analysis using an annular four-channel silicon drift detector. *Microscopy Today* **25**, 30–35 (2017).
66. D. N. Simkus, J. C. Aponte, J. E. Elsila, E. T. Parker, D. P. Glavin, J. P. Dworkin, Methodologies for analyzing soluble organic compounds in extraterrestrial samples: Amino acids, amines, monocarboxylic acids, aldehydes, and ketones. *Life (Basel)* **9**, 47 (2019).

67. D. J. Creek, A. Jankevics, K. E. Burgess, R. Breitling, M. P. Barrett, IDEOM: An excel interface for analysis of LC-MS-based metabolomics data. *Bioinformatics* **28**, 1048–1049 (2012).
68. C. A. Smith, E. J. Want, G. O'Maille, R. Abagyan, G. Siuzdak, XCMS: Processing mass spectrometry data for metabolite profiling using nonlinear peak alignment, matching, and identification. *Anal. Chem.* **78**, 779–787 (2006).
69. R. A. Scheltema, A. Jankevics, R. C. Jansen, M. A. Swertz, R. Breitling, PeakML/mzMatch: A file format, Java Library, R library, and tool-chain for mass spectrometry data analysis. *Anal. Chem.* **83**, 2786–2793 (2011).
70. Y. Gloaguen, F. Morton, R. Daly, R. Gurden, S. Rogers, J. Wandy, D. Wilson, M. Barrett, K. Burgess, PiMP my metabolome: An integrated, web-based tool for LC-MS metabolomics data. *Bioinformatics* **33**, 4007–4009 (2017).
71. J. Xia, N. Psychogios, N. Young, D. S. Wishart, MetaboAnalyst: A web server for metabolomic data analysis and interpretation. *Nucleic Acids Res.* **37**, W652–W660 (2009).
72. D. Vida, P. S. Gural, P. G. Brown, M. Campbell-Brown, P. Wiegert, Estimating trajectories of meteors: An observational Monte Carlo approach—I. Theory. *Mon. Notices Royal Astron. Soc.* **491**, 2688–2705 (2020).
73. P. Spurný, J. Borovička, J. Kac, P. Kalenda, J. Atanackov, G. Kladnik, D. Heinlein, T. Grau, Analysis of instrumental observations of the Jesenice meteorite fall on April 9, 2009. *Meteorit. Planet. Sci.* **45**, 1392–1407 (2010).
74. H. A. R. Devillepoix, E. K. Sansom, P. A. Bland, M. C. Towner, M. Cupák, R. M. Howie, T. Jansen-Sturgeon, M. A. Cox, B. A. D. Hartig, G. K. Benedix, J. P. Paxman, The dingle dell meteorite: A halloween treat from the main belt. *Meteorit. Planet. Sci.* **53**, 2212–2227 (2018).
75. E. K. Sansom, T. Jansen-Sturgeon, M. G. Rutten, H. A. R. Devillepoix, P. A. Bland, R. M. Howie, M. A. Cox, M. C. Towner, M. Cupák, B. A. D. Hartig, 3D meteoroid trajectories. *Icarus* **321**, 388–406 (2019).
76. P. Spurný, J. Borovička, L. Shrbený, The Žďár nad Sázavou meteorite fall: Fireball trajectory, photometry, dynamics, fragmentation, orbit, and meteorite recovery. *Meteorit. Planet. Sci.* **55**, 376–401 (2020).
77. J. Borovička, J. Tóth, A. Igaz, P. Spurný, P. Kalenda, J. Haloda, J. Svoreň, L. Kornoš, E. Silber, P. Brown, M. Husárik, The Košice meteorite fall: Atmospheric trajectory, fragmentation, and orbit. *Meteorit. Planet. Sci.* **48**, 1757–1779 (2013).
78. R. J. Macke, G. J. Consolmagno, D. T. Britt, Density, porosity, and magnetic susceptibility of carbonaceous chondrites. *Meteorit. Planet. Sci.* **46**, 1842–1862 (2011).
79. H. Rein, D. S. Spiegel, IAS15: A fast, adaptive, high-order integrator for gravitational dynamics, accurate to machine precision over a billion orbits. *MNRAS* **446**, 1424–1437 (2015).
80. C. M. Pieters, L. A. Taylor, S. K. Noble, L. P. Keller, B. Hapke, R. V. Morris, C. C. Allen, D. S. McKay, S. Wentworth, Space weathering on airless bodies: Resolving a mystery with lunar samples. *Meteorit. Planet. Sci.* **35**, 1101–1107 (2000).
81. H. C. Bates, A. J. King, K. L. Donaldson Hanna, N. E. Bowles, S. S. Russell, Linking mineralogy and spectroscopy of highly aqueously altered CM and CI carbonaceous chondrites in preparation for primitive asteroid sample return. *Meteorit. Planet. Sci.* **55**, 77–101 (2020).
82. H. Busemann, H. Baur, R. Wieler, Primordial noble gases in "phase Q" in carbonaceous and ordinary chondrites studied by closed system stepped etching. *Meteorit. Planet. Sci.* **35**, 949–973 (2000).
83. G. R. Huss, R. S. Lewis, Noble gases in presolar diamonds I: Three distinct components and their implications for diamond origins. *Meteoritics* **29**, 791–810 (1994).
84. I. Leya, J. Masarik, Cosmogenic nuclides in stony meteorites revisited. *Meteorit. Planet. Sci.* **44**, 1061–1086 (2009).
85. C. M. O'. D. Alexander, Quantitative models for the elemental and isotope fractionation in chondrites: The carbonaceous chondrites. *Geochim. Cosmochim. Acta* **254**, 277–309 (2019).
86. N. Bhandari, S. V. S. Murty, P. N. Shukla, A. D. Shukla, R. R. Mahajan, M. M. Sarin, G. Srinivasan, K. M. Suthar, M. S. Sisodia, S. Jha, A. Bischoff, Itawa Bhopji (L3-5) chondrite regolith breccia: Fall, classification and cosmogenic records. *Meteorit. Planet. Sci.* **37**, 549–563 (2002).
87. P. P. Povinec, J. Masarik, I. Sýkora, A. Kováčik, J. Beňo, M. Laubenstein, V. Porubčan, Cosmogenic nuclides in the Košice meteorite: Experimental investigations and Monte Carlo simulations. *Meteorit. Planet. Sci.* **50**, 880–892 (2015).
88. N. Braukmüller, F. Wombacher, D. C. Hezel, R. Escoube, C. Münker, The chemical composition of carbonaceous chondrites: Implications for volatile element depletion, complementarity and alteration. *Geochim. Cosmochim. Acta* **239**, 17–48 (2018).
89. M. S. Spergel, R. C. Reedy, O. W. Lazareth, P. W. Levy, L. A. Slatest, Cosmogenic neutron-capture-produced nucleides in stony meteorites. *J. Geophys. Res. Suppl.* **91**, D483–D494 (1986).
90. R. Wieler, T. Graf, P. Signer, S. Vogt, G. F. Herzog, C. Tuniz, D. Fink, L. K. Fifield, J. Klein, R. Middleton, A. J. T. Jull, P. Pellas, J. Masarik, G. Dreibus, Exposure history of the Torino meteorite. *Meteorit. Planet. Sci.* **31**, 265–272 (1996).
91. G. F. Herzog, Cosmic-ray exposure ages of meteorites, in *Treatise on Geochmistry*, H. D. Holland, K. K. Turekian, Eds. (Elsevier, 2003), vol. 1.
92. T. Schulz, P. P. Povinec, L. Ferrière, A. J. T. Jull, A. Kováčik, I. Sýkora, J. Tusch, C. Münker, D. Topa, C. Koeberl, The history of the Tissint meteorite, from its crystallization on Mars to its exposure in space: New geochemical, isotopic, and cosmogenic nuclide data. *Meteorit. Planet. Sci.* **55**, 294–311 (2020).
93. K. T. Howard, C. M. O'. D. Alexander, D. L. Schrader, K. Dyl, Classification of hydrous meteorites (CR, CM and C2 ungrouped) by phyllosilicate fraction: PSD-XRD model mineralogy and planetesimal environments. *Geochim. Cosmochim. Acta* **149**, 206–222 (2015).
94. M. R. Lee, P. Lindgren, M. R. Sofe, Aragonite, breunnerite, calcite and dolomite in the CM carbonaceous chondrites: High fidelity recorders of progressive parent body aqueous alteration. *Geochim. Cosmochim. Acta* **144**, 126–156 (2014).
95. D. J. Barber, Phyllosilicates and other layer-structured materials in stony meteorites. *Clay Miner.* **20**, 415–454 (1985).
96. I. D. R. Mackinnon, M. E. Zolensky, Proposed structures for poorly characterized phases in C2M carbonaceous chondrite meteorites. *Nature* **309**, 240–242 (1984).
97. P. Rochette, J. Gattacceca, L. Bonal, M. Bourot-Denise, V. Chevrier, J. Clerc, G. Consolmagno, L. Folco, M. Gounelle, T. Kohout, L. Pesonen, E. Quirico, L. Sagnotti, A. Skripnik, Magnetic classification of stony meteorites: 2. Non-ordinary chondrites. *Meteorit. Planet. Sci.* **43**, 959–980 (2008).
98. C. Cournède, J. Gattacceca, M. Gounelle, P. Rochette, B. Weiss, B. Zanda, An early solar system magnetic field recorded in CM chondrites. *Earth Planet. Sci. Lett.* **410**, 62–74 (2015).
99. R. Harrison, I. Lascu, FORCulator: A micromagnetic tool for simulating first-order reversal curve diagrams. *Geochem. Geophys. Geosyst.* **15**, 4671–4691 (2014).
100. R. Harrison, X. Zhao, P. Hu, T. Sata, D. Heslop, A. Muxworthy, H. Oda, V. Kuppili, A. Roberts, Simulation of remanent, transient, and induced first-order reversal curve (FORC) diagrams for interacting particles with uniaxial, cubic, and hexagonal anisotropy. *J. Geophys. Res. Solid Earth* **124**, 1404–1429 (2019).
101. J. Bryson, B. Weiss, J. Biersteker, A. King, S. Russell, Constraints on the distances and timescales of solid migration in the early solar system from meteorite magnetism. *Astrophys. J.* **869**, 103 (2020).
102. J. Bryson, B. Weiss, E. Lima, J. Gattacceca, W. Cassata, Evidence for asteroid scattering and distal solar system solids from meteorite paleomagnetism. *Astrophys. J.* **892**, 126 (2020).
103. V. K. Pearson, M. A. Sephton, I. A. Franchi, J. M. Gibson, I. Gilmour, Carbon and nitrogen in carbonaceous chondrites: Elemental abundances and stable isotopic compositions. *Meteorit. Planet. Sci.* **41**, 1899–1918 (2006).
104. C. M. O'. D. Alexander, S. S. Russell, J. W. Arden, R. D. Ash, M. M. Grady, C. T. Pillinger, The origin of chondritic macromolecular matter: A carbon and nitrogen isotope study. *Meteorit. Planet. Sci.* **33**, 603–622 (1998).
105. S. S. Russell, J. W. Arden, C. T. Pillinger, A carbon and nitrogen isotope study of diamond from primitive chondrites. *Meteorit. Planet. Sci.* **31**, 343–355 (1996).
106. M. M. Grady, I. P. Wright, P. K. Swart, C. T. Pillinger, The carbon and oxygen isotopic composition of meteoritic carbonates. *Geochim. Cosmochim. Acta* **52**, 2855–2866 (1988).
107. M. M. Grady, A. B. Verchovsky, I. A. Franchi, I. P. Wright, C. T. Pillinger, Light dement geochemistry of the Tagish Lake CI2 chondrite: Comparison with CI1 and CM2 meteorites. *Meteorit. Planet. Sci.* **37**, 713–735 (2002).
108. M. A. Sephton, Organic geochemistry of meteorites, in *Treatise on Geochmistry* (Elsevier, ed. 2, 2014), vol. 1, chap. 12.
109. M. A. Sephton, A. B. Verchovsky, P. A. Bland, I. Gilmour, M. M. Grady, I. P. Wright, Investigating the variations in carbon and nitrogen isotopes in carbonaceous chondrites. *Geochim. Cosmochim. Acta* **67**, 2093–2108 (2003).
110. E. Mazor, D. Heymann, E. Anders, Noble gases in carbonaceous chondrites. *Geochim. Cosmochim. Acta* **34**, 781–824 (1970).
111. A. Boosman, I. L. ten Kate, P. Mason, L. Polerecky, D. Materic, R. Hilzinger, T. Rockmann, UV induced methane and volatile organic carbon emission from the Murchison meteorite. *EPSC Abstr.* **12**, EPSC2018-663 (2018).
112. J. G. Lawless, G. U. Yuen, Quantification of monocarboxylic acids in the Murchison carbonaceous meteorite. *Nature* **282**, 396–398 (1979).
113. G. W. Cooper, W. M. Onwo, J. R. Cronin, Alkyl phosphonic acids and sulfonic acids in the Murchison meteorite. *Geochim. Cosmochim. Acta* **56**, 4109–4115 (1992).
114. D. P. Glavin, J. P. Dworkin, A. Aubrey, O. Botta, J. H. Doty III, Z. Martins, J. L. Bada, Amino acid analyses of Antarctic CM2 meteorites using liquid chromatography-time of flight-mass spectrometry. *Meteorit. Planet. Sci.* **41**, 889–902 (2006).
115. V. S. Heber, R. Wieler, H. Baur, C. Olinger, D. Burnett, Noble gas composition of the solar wind as collected by the Genesis mission. *Geochim. Cosmochim. Acta* **73**, 7414–7432 (2012).

116. D. Györe, A. Tait, D. I. Hamilton, F. M. Stuart, The formation of NeH^+ in static vacuum mass spectrometers and re-determination of $^{21}Ne/^{20}Ne$ of air. *Geochim. Cosmochim. Acta* **263**, 1–12 (2019).
117. R. Wieler, Cosmic ray-produced noble gases in meteorites. *Rev. Mineral. Geochem.* **47**, 125–170 (2002).
118. N. Dauphas, The isotopic nature of the Earth's accreting material through time. *Nature* **541**, 521–524 (2017).
119. A. Meshik, C. Hohenberg, O. Pravdivtseva, D. Burnett, Measuring the isotopic composition of solar wind noble gases, in *Exploring the Solar Wind*, M. Lasar, Ed. (InTech, Croatia,2012), pp. 93–121.
120. R. Wieler, E. Anders, H. Baur, R. S. Lewis, P. Signer, Characterisation of Q-gases and other noble gas components in the Murchison meteorite. *Geochim. Cosmochim. Acta* **56**, 2907–2921 (1992).

Acknowledgments: We are extremely grateful to the local communities in Winchcombe, Woodmancote, and the surrounding area. The fall of the Winchcombe meteorite happened during the COVID-19 pandemic and a national lockdown in the United Kingdom; without their warm welcome, sense of curiosity, and enthusiasm, its rapid recovery would not have been possible. We would also like to thank the wider teams at the Natural History Museum (NHM), London; University of Glasgow; University of Manchester; Open University; and University of Plymouth, who worked tirelessly behind the scenes to ensure that many of us could travel to the fall site. D. and V. Carrick are thanked for their generous donation of a Winchcombe meteorite sample to the NHM, and G. Ensor, L. Jackson, and C. Casey for continuing the search and sharing details of later finds. We thank the citizen-scientists of the UK Meteor Network (UKMON), the Network for Meteor Triangulation and Orbit Determination (NEMETODE), the UK Fireball Network (UKFN), the Fireball Recovery and InterPlanetary Observation Network (FRIPON), the Global Meteor Network (GMN), and the AllSky7 network for watching the skies over the United Kingdom. M. Anand is thanked for logistical support in the weeks after the fall. J. Najorka and J. Spratt at the NHM, and the Imaging Spectroscopy and Analysis Center (ISAAC) and Kelvin Nanocharacterization Center at the University of Glasgow, are thanked for analytical support. **Funding:** This study was supported by urgency funding from the U.K.'s Science and Technology Facilities Council (STFC) as part of the project "Curation and Preliminary Examination of the Winchcombe Carbonaceous Chondrite Fall." Additional work was funded by STFC through grants ST/N000846/1, ST/T002328/1, ST/T506096/1, and ST/W001128/1 (to L.D., M.R.L., and L.J.Ha.); ST/V000675/1 (to K.H.J. and R.H.J.); ST/P005225/1 (to R.T.); ST/S000348/1 (to M.V.G., P.J.W., and M.J.B.); ST/R00143X/1 (to J.B. and L.J.Hi.); ST/S000615/1 (to G.S.C.); ST/V000799/1 (to P.G.); and ST/V000888/1 (to T.E.). A.J.K. and H.C.B. acknowledge funding support from UK Research and Innovation (UKRI) grant MR/T020261/1. P.L.C. acknowledges funding support from UKRI grant MR/S03465X/1. K.H.J. acknowledges funding support from the Royal Society, grant URF\R\201009. L.J.Ha. and M.R.L. acknowledge funding from Natural Environment Research Council (NERC) National Environmental Isotope Facility (NEIF) grant no. 2406.0321. L.D., M.R.L., and L.J.Ha. acknowledge COVID-19 funding support from the University of Glasgow, UK. D.V. was supported in part by NASA cooperative agreement 80NSSC21M0073. P.P. and I.Sy. acknowledge funding from the VEGA agency, project no.1/0421/20. A.J.T.J. acknowledges support from the European Union and the State of Hungary, cofinanced by the European Regional Development Fund in the project of GINOP-2.3.2-15-2016-00009 "ICER." P.M.S. acknowledges support from the European Union's Horizon 2020 research and innovation programme under the Marie Sklodowska-Curie grant agreement no. 945298. FRIPON was initiated by funding from ANR (grant N.13-BS05-0009-03), carried out by the Paris Observatory, Muséum National d'Histoire Naturelle, Paris-Saclay University, and Institut Pythéas (LAM-CEREGE). FRIPON data are hosted and processed at Institut Pythéas SIP (Service Informatique Pythéas). The Desert Fireball Network team and Global Fireball Observatory are funded by the Australian Research Council (DP200102073). **Author contributions:** The overall study design, analytical campaign, and preparation of the manuscript were led by A.J.K., L.D., K.H.J., R.C.G., H.A.R.D., M.D.S., Q.H.S.C., S.S.R., H.C.B., J.F.J.B., and P.L.C. Collection, analysis, and interpretation were performed: (i) fireball data by D.V., E.K.S., M.C.T., M.C., P.M.S., P.A.B., R.K., P.C.-B., F.C., B.Z., P.V., S.Bou., M.H., G.S.C., J.S.Y., C.S., J.H., D.J., N.J., S.Bos., A.S., P.D., I.M., D.R., A.R.D.S., B.S., R.B., M.M., A.A.S., R.Fl., L.Ba., and J.R.; (ii) electron microscopy data by M.R.L., N.R.S., R.T., M.V.G., J.B., L.J.Hi., R.H.J., J.T.M., M.J.G., L.J., P.-E.M., T.S., F.M.W., C.S.H., D.H., P.J.W., M.J.B., L.S.A., A.D., L.T.C., and V.S.; (iii) cosmogenic nuclide data by P.P., M.L., D.Sa., A.C., T.J.W., and I.Sy.; (iv) IR data by K.A.S., R.J.C., T.J.W., and N.E.B.; (v) CT data by C.J.F., N.V.A., and B.C.; (vi) carbon and nitrogen data by A.B.V., F.A.J.A., and M.M.G.; (vii) neon isotope data by F.M.St., L.D.N., and D.G.; (viii) oxygen isotope data by R.Fi. and I.A.F.; (ix) titanium isotope data by K.M.M.S. and T.E.; (x) chromium isotope data by R.C.J.S.; (xi) LC-MS data by A.O. and L.J.Ha.; (xii) GC-MS data by M.A.S. and J.S.W.; (xiii) magnetic data by S.S. and R.J.H.; (xiv) SIFT-MS data by G.H.M. and M.J.P.; (xv) ICP-MS data by E.R.H.-W.; (xvi) XRD data by P.F.S.; (xvii) hydrogen pyrolysis by A.J.B. M.B.I., S.Mc., S.J.B., Z.I.D., P.G., A.E.P., C.J.W., F.M.Su., S.F., I.Sp., S.N., B.M., D.Sk., D.K., A.M., S.Mo., S.E.M., P.M.G., L.Bo., V.B., C.W., H.W., and R.W. played a substantial role in the recovery of the Winchcombe meteorite, and C.S. provided logistics and curatorial support. All authors contributed to the final edit of the manuscript. **Competing interests:** The authors declare that they have no competing interests. **Data and materials availability:** All data needed to evaluate the conclusions in the paper are present in the paper and/or the Supplementary Materials.

Submitted 5 April 2022
Accepted 20 October 2022
Published 16 November 2022
10.1126/sciadv.abq3925

ScienceAdvances

The Winchcombe meteorite, a unique and pristine witness from the outer solar system

Ashley J. KingLuke DalyJames RoweKatherine H. JoyRichard C. GreenwoodHadrien A. R. DevillepoixMartin D. SuttleQueenie H. S. ChanSara S. RussellHelena C. BatesJames F. J. BrysonPatricia L. ClayDenis VidaMartin R. LeeÁine O'BrienLydia J. HallisNatasha R. StephenRomain TartèseEleanor K. SansomMartin C. TownerMartin CupakPatrick M. ShoberPhil A. BlandRoss FindlayIan A. FranchiAlexander B. VerchovskyFeargus A. J. AbernethyMonica M. GradyCameron J. FloydMatthias Van GinnekenJohn BridgesLeon J. HicksRhian H. JonesJennifer T. MitchellMatthew J. GengeLaura JenkinsPierre-Etienne MartinMark A. SephtonJonathan S. WatsonTobias SalgeKatherine A. ShirleyRowan J. CurtisTristram J. WarrenNeil E. BowlesFinlay M. StuartLuigia Di NicolaDomokos GyöreAdrian J. BoyceKathryn M. M. ShawTim ElliottRobert C. J. SteelePavel PovinecMatthias LaubensteinDavid SandersonAlan CresswellAnthony J. T. JullIvan SýkoraSanjana SridharRichard J. HarrisonFrancesca M. WillcocksCatherine S. HarrisonDaniel HallattPenny J. WozniakiewiczMark J. BurchellLuke S. AlesbrookAishling DignamNatasha V. AlmeidaCaroline L. SmithBrett ClarkEmma R. Humphreys-WilliamsPaul F. SchofieldLuke T. CornwellVassilia SpathisGeraint H. MorganMark J. PerkinsRichard KacerekPeter Campbell-BurnsFrancois ColasBrigitte ZandaPierre VernazzaSylvain BouleySimon JeanneMike HankeyGareth S. CollinsJohn S. YoungClive ShawJana HorakDave JonesNick JamesSteve BosleyAlan ShuttleworthPaul DickinsonIan McMullanDerek RobsonAndrew R. D. SmedleyBen StanleyRichard BassomMark McIntyreAdam A. SuttleRichard FleetLuc BastiaensMíra B. IhászSarah McMullanSarah J. BoazmanZach I. DickesonPeter M. GrindrodAnnemarie E. PickersgillColin J. WeirFiona M. SuttleSarah FarrellyIeun SpencerSheeraz NaqviBen MayneDan SkiltonDan KirkAnn MounseySally E. MounseySarah MounseyPamela GodfreyLachlan BondVictoria BondCathryn WilcockHannah WilcockRob Wilcock

Sci. Adv., 8 (46), eabq3925. • DOI: 10.1126/sciadv.abq3925